

## FD3D\_TSN - Theoretical background

Authors: Jan Premus, František Gallovič,  
Ladislav Hanyk, Alice-Agnes Gabriel

# 1. Wave propagation in the elastic medium

## 1.1 Elastodynamic equation and Hooke's law

The state of an elastic medium is described by two fields – displacement field  $u_i$  and stress field  $\sigma_{ij}$ . Indices  $i, j$  denote a component of a given vector or tensor and can have values of 1, 2 and 3 for  $x, y$  and  $z$  components, respectively. Time development of both fields is governed by two equations – the elastodynamic equation

$$\rho \frac{\partial^2 u_i}{\partial t^2} = \sigma_{ij,j}, \quad (1.1)$$

and Hooke's law

$$\sigma_{ij} = c_{ijkl} u_{k,l}. \quad (1.2)$$

Einstein summation is assumed, unless stated otherwise. Spatially variable parameters  $\rho$  (density) and  $c_{ijkl}$  (tensor of elastic moduli) describe material properties. Only isotropic material will be presumed in this work, therefore

$$c_{ijkl} = \lambda \delta_{ij} \delta_{kl} + \mu (\delta_{ik} \delta_{jl} + \delta_{il} \delta_{jk}), \quad (1.3)$$

where  $\lambda$  and  $\mu$  are Lamé's parameters.

Using the combination of equations (1.1) and (1.2) for the description of the wave propagation is called displacement-stress formulation. Extensively used alternative is the velocity-stress formulation [Moczo et al., 2007], which leads to a more symmetric set of equations and will be used throughout this work. Velocity  $v_i$  is substituted into the elastodynamic equation as the time derivative of the displacement:

$$\rho \frac{\partial v_i}{\partial t} = \sigma_{ij,j}, \quad (1.4)$$

and Hooke's law is differentiated with respect to time:

$$\frac{\partial \sigma_{ij}}{\partial t} = c_{ijkl} v_{k,l}. \quad (1.5)$$

In the frequency domain, this set of equations has the following form:

$$\rho \iota \omega \hat{v}_i = \hat{\sigma}_{ij,j} \quad (1.6)$$

$$\iota \omega \hat{\sigma}_{ij} = c_{ijkl} \hat{v}_{k,l}, \quad (1.7)$$

where  $\hat{v}_i$  and  $\hat{\sigma}_{ij}$  are velocity and stress as a function of angular frequency  $\omega$  and  $\iota$  an imaginary unit.

One of the analytical solutions of the elastodynamic equation can be found in the form of a plane wave

$$v_j = V_j \exp[-\iota(k_1 x_1 + k_2 x_2 + k_3 x_3 - \omega t)], \quad (1.8)$$

where  $V_j$  represents the amplitude of the  $j$ -th component of the plane wave solution,  $\mathbf{k} = (k_1, k_2, k_3)$  is a wave vector.

## 1.2 Grid and finite differences

All calculations will be performed using a three dimensional Cartesian coordinate system  $(x, y, z)$  with forth dimension being time  $t$ . The space is discretized into a grid of discrete points numbered by four indexes  $(I, J, K, N)$ . Position of a point is given by four values –  $(x_I, y_J, z_K, t_N)$ . Only regular grids will be considered, which means that for each  $I, J, K, N$  applies:

$$x_I - x_{I-1} = \Delta h \quad (1.9)$$

$$y_J - y_{J-1} = \Delta h \quad (1.10)$$

$$z_K - z_{K-1} = \Delta h \quad (1.11)$$

$$t_N - t_{N-1} = \Delta t, \quad (1.12)$$

where  $\Delta h$  is a spatial and  $\Delta t$  temporal grid spacing. The position of the node will be given by four numbers  $I, J, K, N$ , that can have half integer values  $0, 1/2, 1, \dots$ . Fields  $v_i$  and  $\sigma_{ij}$  are approximated by their values at these discrete nodes. They can be calculated all at same point (unstaggered grid) or at different points mutually shifted (staggered grid). Partly staggered grids, where all velocity components are at one point and all stress components at another were also used, especially when attenuation came into consideration.

Mutual positions of the components in the staggered grid is shown in Fig 1.1. These positions are chosen with respect to the discretization of the spatial derivatives in the elastodynamic equation and the Hooke's law.

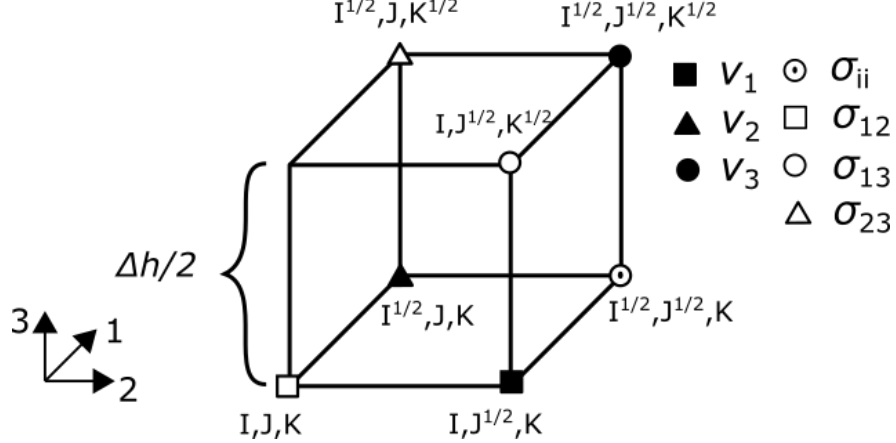


Figure 1.1: Staggered grid cell positioned around the node  $I, J, K$  considered in this Thesis. Symbols (triangles, squares, circles) label the positions of spatially staggered velocity and stress components.

The position of the velocity and stress components is staggered in time also. All velocity components are calculated at  $N\Delta t$  time levels, for  $N = 0, 1, \dots, T/\Delta t$ , where  $T$  is the maximum simulation time. The stress components are positioned at the time levels shifted by a factor of  $\Delta t/2$  as can be seen in Fig 1.2.

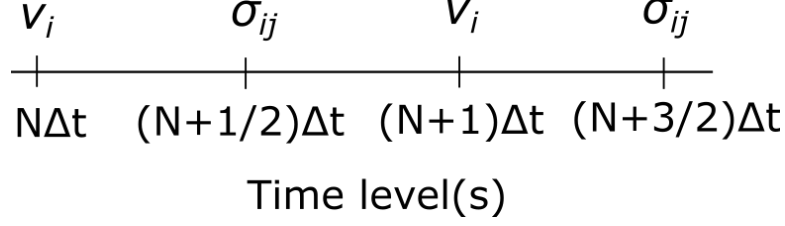


Figure 1.2: Time staggered position of the velocity and stress components.

Solving the set of partial differential equations (1.4) and (1.5) by the finite difference (FD) method requires approximation of the time and spatial derivatives by respective FD formulas. FD formulas of the second order read:

$$(D_1^{(2)}\phi)_{I,J,K} = \left[ \phi_{I^{\frac{1}{2}},J,K} - \phi_{I^{-\frac{1}{2}},J,K} \right] / \Delta h \quad (1.13)$$

$$(D_2^{(2)}\phi)_{I,J,K} = \left[ \phi_{I,J^{\frac{1}{2}},K} - \phi_{I,J^{-\frac{1}{2}},K} \right] / \Delta h \quad (1.14)$$

$$(D_3^{(2)}\phi)_{I,J,K} = \left[ \phi_{I,J,K^{\frac{1}{2}}} - \phi_{I,J,K^{-\frac{1}{2}}} \right] / \Delta h. \quad (1.15)$$

And FD formulas of the forth order read:

$$(D_1^{(4)}\phi)_{I,J,K} = \left[ \frac{9}{8}(\phi_{I^{\frac{1}{2}},J,K} - \phi_{I^{-\frac{1}{2}},J,K}) - \frac{1}{24}(\phi_{I^{\frac{3}{2}},J,K} - \phi_{I^{-\frac{3}{2}},J,K}) \right] / \Delta h \quad (1.16)$$

$$(D_2^{(4)}\phi)_{I,J,K} = \left[ \frac{9}{8}(\phi_{I,J^{\frac{1}{2}},K} - \phi_{I,J^{-\frac{1}{2}},K}) - \frac{1}{24}(\phi_{I,J^{\frac{3}{2}},K} - \phi_{I,J^{-\frac{3}{2}},K}) \right] / \Delta h \quad (1.17)$$

$$(D_3^{(4)}\phi)_{I,J,K} = \left[ \frac{9}{8}(\phi_{I,J,K^{\frac{1}{2}}} - \phi_{I,J,K^{-\frac{1}{2}}}) - \frac{1}{24}(\phi_{I,J,K^{\frac{3}{2}}} - \phi_{I,J,K^{-\frac{3}{2}}}) \right] / \Delta h, \quad (1.18)$$

where  $\phi$  denotes any components of velocity or stress. For convinience we use  $I^J$  instead of  $I + J$  to express complicated indexes designating position in the FD grid. The direction of the difference is set by a lower index (1 for  $x$ , etc.).

The position in time will be marked by an upper index, where index  $N$  marks the time level  $N\Delta t$ . The time difference  $D_t\phi$  at the time level  $(N + \frac{1}{2})\Delta t$  will be defined as a difference between values of  $\phi$  at time levels shifted by  $\Delta t/2$  in both directions:

$$(D_t\phi)_{I,J,K}^{N\frac{1}{2}} = \left[ \phi_{I,J,K}^N - \phi_{I,J,K}^{N-1} \right] / \Delta t. \quad (1.19)$$

This central finite difference formula is of the second order.

Using (1.16,1.17,1.18) and (1.19) to approximate the spatial and time derivatives in (1.4) and (1.5) leads to an updating scheme that allows for calculation of  $\sigma_{ij}^{N\frac{1}{2}}$  and  $v_i^{N+1}$  from  $\sigma_{ij}^{N-\frac{1}{2}}$  and  $v_i^N$ . As a starting point, the initial conditions  $\sigma_{ij}^{\frac{1}{2}}$  and  $v_i^0$  for velocity and stress, respectively, are required .

The scheme using the 2-nd order spatial formulas was introduced by [Virieux, 1986] and using the 4-th order formulas by [Levander, 1988], in both cases only for calculation of P-SV seismograms, not the whole elastodynamic equation. The

full staggered FD 4-th order scheme used in this work was introduced by [Graves, 1996]. It consists of nine FD formulas:

$$(v_1)_{I,J\frac{1}{2},K}^{N^1} = (v_1)_{I,J\frac{1}{2},K}^N + \frac{\Delta t}{\rho} \left( [D_1^{(4)}\sigma_{11}]_{I,J\frac{1}{2},K} + [D_2^{(4)}\sigma_{12}]_{I,J\frac{1}{2},K} + [D_3^{(4)}\sigma_{13}]_{I,J\frac{1}{2},K} \right) \quad (1.20)$$

$$(v_2)_{I\frac{1}{2},J,K}^{N^1} = (v_2)_{I\frac{1}{2},J,K}^N + \frac{\Delta t}{\rho} \left( [D_1^{(4)}\sigma_{12}]_{I\frac{1}{2},J,K} + [D_2^{(4)}\sigma_{22}]_{I\frac{1}{2},J,K} + [D_3^{(4)}\sigma_{23}]_{I\frac{1}{2},J,K} \right) \quad (1.21)$$

$$(v_3)_{I\frac{1}{2},J\frac{1}{2},K\frac{1}{2}}^{N^1} = (v_3)_{I\frac{1}{2},J\frac{1}{2},K\frac{1}{2}}^N + \frac{\Delta t}{\rho} \left( [D_1^{(4)}\sigma_{13}]_{I\frac{1}{2},J\frac{1}{2},K\frac{1}{2}} + [D_2^{(4)}\sigma_{23}]_{I\frac{1}{2},J\frac{1}{2},K\frac{1}{2}} + [D_3^{(4)}\sigma_{33}]_{I\frac{1}{2},J\frac{1}{2},K\frac{1}{2}} \right) \quad (1.22)$$

$$(\sigma_{11})_{I\frac{1}{2},J\frac{1}{2},K}^{N\frac{1}{2}} = (\sigma_{11})_{I\frac{1}{2},J\frac{1}{2},K}^{N-\frac{1}{2}} + \Delta t \left( (\lambda + 2\mu)[D_1^{(4)}v_1]_{I\frac{1}{2},J\frac{1}{2},K} + \lambda[D_2^{(4)}v_2]_{I\frac{1}{2},J\frac{1}{2},K} + \lambda[D_3^{(4)}v_3]_{I\frac{1}{2},J\frac{1}{2},K} \right) \quad (1.23)$$

$$(\sigma_{22})_{I\frac{1}{2},J\frac{1}{2},K}^{N\frac{1}{2}} = (\sigma_{22})_{I\frac{1}{2},J\frac{1}{2},K}^{N-\frac{1}{2}} + \Delta t \left( \lambda[D_1^{(4)}v_1]_{I\frac{1}{2},J\frac{1}{2},K} + (\lambda + 2\mu)[D_2^{(4)}v_2]_{I\frac{1}{2},J\frac{1}{2},K} + \lambda[D_3^{(4)}v_3]_{I\frac{1}{2},J\frac{1}{2},K} \right) \quad (1.24)$$

$$(\sigma_{33})_{I\frac{1}{2},J\frac{1}{2},K}^{N\frac{1}{2}} = (\sigma_{33})_{I\frac{1}{2},J\frac{1}{2},K}^{N-\frac{1}{2}} + \Delta t \left( \lambda[D_1^{(4)}v_1]_{I\frac{1}{2},J\frac{1}{2},K} + \lambda[D_2^{(4)}v_2]_{I\frac{1}{2},J\frac{1}{2},K} + (\lambda + 2\mu)[D_3^{(4)}v_3]_{I\frac{1}{2},J\frac{1}{2},K} \right) \quad (1.25)$$

$$(\sigma_{12})_{I,J,K}^{N\frac{1}{2}} = (\sigma_{12})_{I,J,K}^{N-\frac{1}{2}} + \mu\Delta t \left( [D_2^{(4)}v_1]_{I,J,K} + [D_1^{(4)}v_2]_{I,J,K} \right) \quad (1.26)$$

$$(\sigma_{13})_{I,J\frac{1}{2},K\frac{1}{2}}^{N\frac{1}{2}} = (\sigma_{13})_{I,J\frac{1}{2},K\frac{1}{2}}^{N-\frac{1}{2}} + \mu\Delta t \left( [D_3^{(4)}v_1]_{I,J\frac{1}{2},K\frac{1}{2}} + [D_1^{(4)}v_3]_{I,J\frac{1}{2},K\frac{1}{2}} \right) \quad (1.27)$$

$$(\sigma_{23})_{I\frac{1}{2},J,K\frac{1}{2}}^{N\frac{1}{2}} = (\sigma_{23})_{I\frac{1}{2},J,K\frac{1}{2}}^{N-\frac{1}{2}} + \mu\Delta t \left( [D_3^{(4)}v_2]_{I\frac{1}{2},J,K\frac{1}{2}} + [D_2^{(4)}v_3]_{I\frac{1}{2},J,K\frac{1}{2}} \right). \quad (1.28)$$

They are derived by the discretization of the elastodynamic equation (1.4) for velocities (1.20 to 1.22), and Hooke's law (1.5) for stress (1.23 to 1.28), for the case of the isotropic material rheology. Formulas are for all velocity and stress components at the nodes in one grid cell, positioned at  $I, J, K$ . The material parameters are considered constant through the cell. Fig (1.1) shows mutual positions of the components in the grid cell.

For the FD scheme to be stable, its plane wave solution (1.8) cannot grow when the propagation of the wave is calculated using the scheme [Moczo et al., 2007]. The ansatz of the solution into the concrete FD scheme (this approach is called the Neumann’s method) leads to a CFL condition (Courant-Friedrichs-Levy) for discretization steps  $\Delta t$  and  $\Delta h$ . In particular, for the time step we obtain [Moczo et al., 2000]

$$\Delta t < C_{CFL} \Delta h, \quad (1.29)$$

where  $C_{CFL}$  is a parameter depending on the particular FD scheme and the wave velocity in a media. The value

$$C_{CFL}^\alpha = \frac{6}{v_{alpha} 7\sqrt{3}}, C_{CFL}^\beta = \frac{6}{v_\beta 7\sqrt{3}} \quad (1.30)$$

was derived by Moczo et al. [2000] for the 4th order staggered grid FD scheme. Velocities of the P and S wave are denoted as  $v_\alpha$  and  $v_\beta$ , respectively. The stability condition (1.29) is more restrictive for the P waves. The time discretization parameter for simulations in heterogenous medium is set to guarantee the stability of the P wave solution in the area with the highest P wave velocity.

The second concept coming from the Neumann’s analysis is the grid dispersion. It offers a way to set  $\Delta h$  to obtain a desired accuracy. The grid dispersion is the ratio between the grid wave velocity ( $v_\alpha^g$  or  $v_\beta^g$ ) at which the wave propagates when FD method is applied and the true wave velocity ( $v_\alpha$  or  $v_\beta$ ). Grid dispersion depends on spatial sampling ratio  $\Delta h/\lambda$ , where  $\lambda = 2\pi v_\alpha(v_\beta)/\omega$  is the wave length of the P(S) wave. The grid dispersion decreases (the discrete wave solution is slowing down) as the spatial sampling ratio increases (less points per wave length). Moczo et al. [2000] recommends setting  $\Delta h$  to have at least 6 grid nodes per wavelength of the S wave at maximum desired frequency. This should bound the error in its velocity by 5 percent.

There are three important concepts in numerical mathematics that need to be taken into account when using discrete PDE methods – consistency, stability and convergence. The FD method is consistent, when its discrete formulas equal the partial differential equations when limiting  $\Delta h, \Delta t \rightarrow 0$ . This is typically the case and it is easy to check.

The FD method is convergent if the discrete solution converges towards the actual solution of the PDE when limiting  $\Delta h, \Delta t \rightarrow 0$ . It is the desired property of FD methods but it is difficult to check, especially when boundary conditions are taken into account.

The FD method is stable, when the discrete solution is bounded, while the actual solution is also bounded. It can be proven, that the FD method is convergent when it is consistent and stable, therefore testing the stability instead of the convergence is possible. Neumann’s method (mentioned above) is a typical method to test boundedness of a solution, although just for the specific shape of the plane wave.

## 2. Dynamic fault model in finite differences

The mathematical description of an approximate earthquake model and its introduction into the FD wave simulation code as a boundary condition are described in this chapter. While earthquake source is a complex set of mechanical (gouge, damage, lubrication), thermal (thermal pressurization, melting) and chemical phenomena, theoretical dynamic earthquake models are much simpler. The popular approximation described here (Section 2.1) sets the earthquake as a shear rupture on a frictional (planar) interface between elastic halfspaces. Higher order effects can be added into this model through more complicated friction law, changes to rheology of the off-fault material, or more complicated geometry of the interface.

We consider two types of friction laws in this Thesis – slip weakening law (Section 2.4) and rate-and-state law. The fact that force required to start the sliding is higher than the force required for its continuation is a major idea behind the slip weakening law. Empirical rate and state (Section 2.5) law considers much wider range of experiments, with sliding velocity changing during the experiment [Dieterich, 1979, Ruina, 1983]. Newer version of this law with fast velocity weakening is considered, based on friction experiments performed at seismic speeds of the order of 1 m/s [Goldsby and Tullis, 2011].

When using staggered/partially staggered grids, components of velocity and stress are not calculated at the same node. Some components will be calculated outside of the fault plane. Historically, there were essentially two groups of methods considered for the introduction of fault boundary into finite differences – inelastic zone methods and split node methods [Moczo et al., 2007].

The first group comprises methods that establish fault as a zone of finite width that surrounds the grid nodes, where velocity and traction is calculated. Their values inside this zone are then considered the same through the zone. Popular methods in this group are thick or thin zone methods (Section 2.2) developed by R. Madariaga.

Splitting the space by the fault into two halves, which are interacting only through chosen nodes at the fault surface is a staple of split node methods. Traction at split node method is described in Section 2.3.

### 2.1 Fault as a boundary condition

Fault plane divides space into two halfspaces, denoted as '+' and '-' as in Fig 2.1. We define slip  $s_i$  as a discontinuity in displacement vector  $u_i$  across the fault

$$s_i(\mathbf{x}, t) = u_i^+(\mathbf{x}, t) - u_i^-(\mathbf{x}, t), \quad (2.1)$$

and slip rate as a discontinuity in velocity

$$\dot{s}_i(\mathbf{x}, t) = v_i^+(\mathbf{x}, t) - v_i^-(\mathbf{x}, t), \quad (2.2)$$

with absolute values denoted as  $s$  and  $\dot{s}$ , respectively.

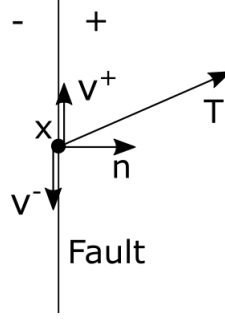


Figure 2.1: Scheme of the fault variables at point  $\mathbf{x}$  – normal to the fault  $n_i$ , discontinuous velocity  $v_i^+$  and  $v_i^-$  and continuous traction  $T_i$ .

Let  $n_i$  be a unit normal vector to the fault, that points into '+' halfspace and  $T_i(\mathbf{x}, \mathbf{n}, t) = \sigma_{ij}n_j$  is a traction on the fault. Since shear faulting is expected, continuity of normal componets of displacement  $u_i^n$  and velocity  $v_i^n$  is in place:

$$0 = u_i^{n+}(\mathbf{x}, t) - u_i^{n-}(\mathbf{x}, t), \quad (2.3)$$

$$0 = v_i^{n+}(\mathbf{x}, t) - v_i^{n-}(\mathbf{x}, t). \quad (2.4)$$

Traction  $T_i(\mathbf{x}, \mathbf{n}, t)$  is continuous through the fault. Let  $S(\mathbf{x}, t)$  be a value of frictional strength. Value of shear traction  $T^s(\mathbf{x}, \mathbf{n}, t)$  at the fault is bounded by frictional strength

$$T^s(\mathbf{x}, t) \leq S(\mathbf{x}, t). \quad (2.5)$$

Second condition on traction requires it to act opposite to velocity discontinuity.

$$T_i^s(\mathbf{x}, t)\dot{s}(\mathbf{x}, t) - S(\mathbf{x}, t)\dot{s}_i(\mathbf{x}, t) = 0 \quad (2.6)$$

The magnitude of traction in this slipping case is set to be equal to frictional strength by condition (2.5). In both following sections trial shear traction  $T_i^T$  is calculated, that equals the values of traction if slip doesn't occur (frictional strength  $S$  higher then  $T^T$ ). For the case of vertical fault, it has only two non-zero components  $T_1^T$  and  $T_3^T$ .

Introduction of the non-planar (or even just dipping planar) fault boundary condition into the regular grid is very complicated. Only Cruz-Atienza et al. [2007] managed to do a stable non-planar model for the case of the partially staggered grid. Irregular grids seem to be the most popular way to introduce the non-planar faults, such as in Duru and Dunham [2016], but these are out of the scope of this work.

Only vertical planar fault will be assumed in this work and all derivations will be done for the fault plane being a 1 – 3 plane. The following symmetries and antisymmetries in stress and velocity components along the fault in 1 – 3 plane are in place (expecting the same material parameters on both sides of the fault plane):

$$v_1^+ = -v_1^- \quad v_2^+ = +v_2^- \quad v_3^+ = -v_3^- \quad (2.7)$$

$$\sigma_{11}^+ = -\sigma_{11}^- \quad \sigma_{22}^+ = \sigma_{22}^- \quad \sigma_{33}^+ = -\sigma_{33}^- \quad (2.8)$$

$$\sigma_{12}^+ = +\sigma_{12}^- \quad \sigma_{13}^+ = -\sigma_{13}^- \quad \sigma_{23}^+ = +\sigma_{23}^- \quad (2.9)$$



## 2.2 Thick and thin zone methods

Formulation of the thick zone method of representation of the fault boundary condition was introduced by Madariaga et al. [1998]. Thin zone method is its improved version, whose accuracy should be better [Madariaga, at <http://www.geologie.ens.fr/~madariag/>].

In both cases, the fault plane is chosen to coincide with one of the 1 – 3 planes in the staggered grid. The position of the plane along axis 2 is denoted as  $J_F$ , which means that for all nodes at the plane  $J = J_F$  applies. The fault boundary condition (2.5, 2.6) is then applied, using appropriate velocity and stress components for traction and slip rate. These components are not all positioned in FD nodes at the fault plane, the value of the component at the closest node is taken instead. The position of fault plane in the FD grid for thick and thin zone method is shown in Fig 2.2.

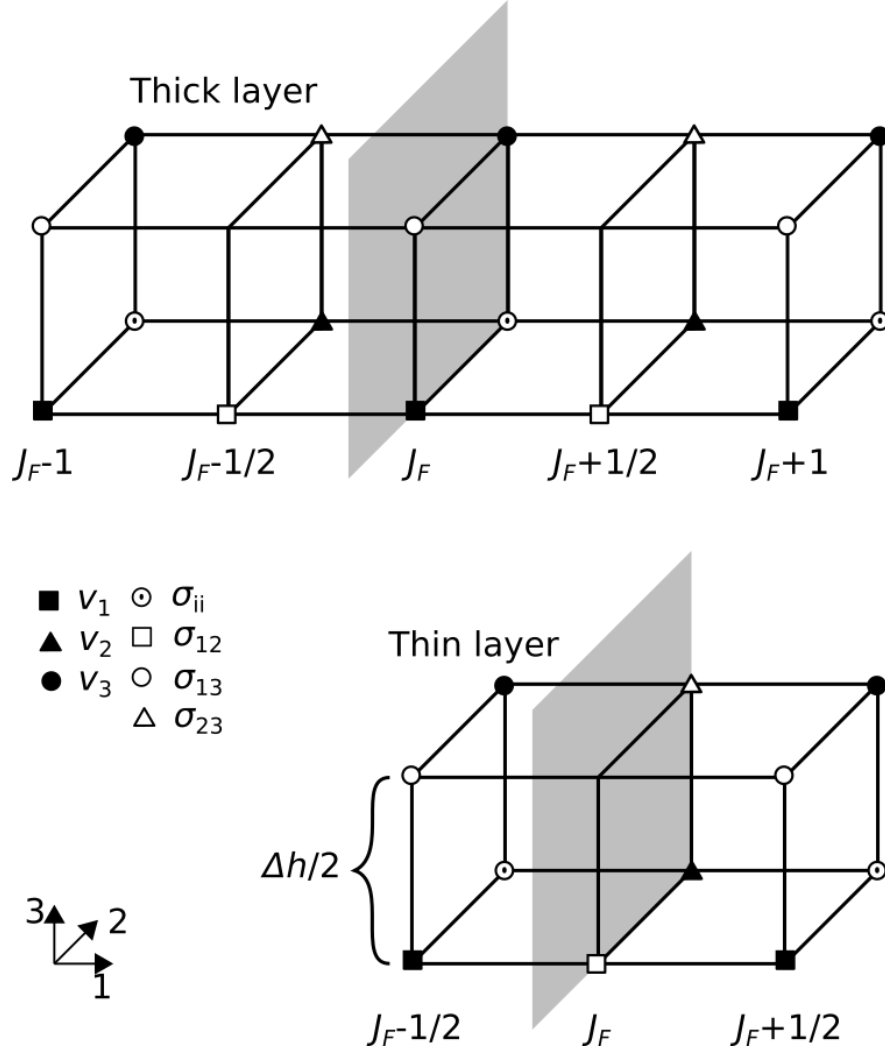


Figure 2.2: Thick and thin layer position in FD staggered grid. The fault plane is denoted by a grey plane at position  $J = J_F$ .

In the thick zone method, the fault plane is set to cut through the finite difference grid in shear velocity nodes ( $v_1$ ,  $v_3$ ). Enforcement of the fault boundary condition using this method requires shear traction components that are cal-

culated at the nodes at the grid plane shifted by  $\Delta h/2$  (stress plane) and shear velocity components at the velocity plane shifted by  $\Delta h$ . Size of the zone containing all components, required for fault boundary condition is  $2\Delta h$ . Assumption, that the traction is the same at the border of the thick zone and in the middle of it, means that inelasticity at the zone around the fault is prescribed. This is only a mathematical approximation, and has no connection to any physical effect in real earthquakes.

First, trial shear traction components are calculated by the FD formula from Hooke's law

$$(T_1^T)^{N\frac{1}{2}}_{I,J_F^{\frac{1}{2}},K} = (\sigma_{12})^{N\frac{1}{2}}_{I,J_F^{\frac{1}{2}},K} = (\mu) \frac{\Delta t}{\Delta h} \left( (D_2^{(4)} v_1)^N_{I,J_F^{\frac{1}{2}},K} + (D_1^{(4)} v_2)^N_{I,J_F^{\frac{1}{2}},K} \right) \quad (2.10)$$

$$(T_3^T)^{N\frac{1}{2}}_{I^{\frac{1}{2}},J_F^{\frac{1}{2}},K^{\frac{1}{2}}} = (\sigma_{23})^{N\frac{1}{2}}_{I^{\frac{1}{2}},J_F^{\frac{1}{2}},K^{\frac{1}{2}}} = \mu \frac{\Delta t}{\Delta h} \left( (D_3^{(4)} v_2)^N_{I^{\frac{1}{2}},J_F^{\frac{1}{2}},K^{\frac{1}{2}}} + (D_2^{(4)} v_3)^N_{I^{\frac{1}{2}},J_F^{\frac{1}{2}},K^{\frac{1}{2}}} \right), \quad (2.11)$$

with traction on the other plane being equal due to the symmetry:

$$(T_1^T)^{N\frac{1}{2}}_{I,J_F^{-\frac{1}{2}},K} = (T_1^T)^{N\frac{1}{2}}_{I,J_F^{\frac{1}{2}},K} \quad (2.12)$$

$$(T_3^T)^{N\frac{1}{2}}_{I^{\frac{1}{2}},J_F^{-\frac{1}{2}},K^{\frac{1}{2}}} = (T_3^T)^{N\frac{1}{2}}_{I^{\frac{1}{2}},J_F^{\frac{1}{2}},K^{\frac{1}{2}}} \quad (2.13)$$

To acquire absolute value of trial traction at both nodes, missing component needs to be interpolated, for example  $T_1^T$  at nodes  $(I^{\frac{1}{2}}, J_F^{\frac{1}{2}}, K^{\frac{1}{2}})$  and  $(I^{\frac{1}{2}}, J_F^{-\frac{1}{2}}, K^{\frac{1}{2}})$ . Alternative approach is to add an extra simplification, by allowing slip only in direction of axis 1 (strike slip) or 3 (dip slip). The value of one component  $T_1^T$  or  $T_3^T$  can then be considered instead of the absolute value of the whole trial shear traction  $(T^T)^{N\frac{1}{2}}$ . The fault conditions (2.5) and (2.6) are then applied to this trial shear traction. The value of the traction is modified to be equal to the friction at all nodes, where it would be larger than friction:

$$(T_i)^{N\frac{1}{2}} = \begin{cases} (T_i^T)^{N\frac{1}{2}}, & \text{if } (T^T)^{N\frac{1}{2}} \leq S^{N\frac{1}{2}} \\ S^{N\frac{1}{2}} \frac{(T_i^T)^{N\frac{1}{2}}}{(T^T)^{N\frac{1}{2}}}, & \text{if } (T^T)^{N\frac{1}{2}} > S^{N\frac{1}{2}}, \end{cases} \quad i = 1, 3. \quad (2.14)$$

Velocity components  $v_1$  and  $v_3$  in planes  $(J_F - 1)$  and  $(J_F + 1)$  are then calculated already with the modified traction. Slip rate components are defined as

$$(\dot{s}_1)^{N^1}_{I,J_F,K} = (v_1)^{N^1}_{I,J_F^1,K} - (v_1)^{N^1}_{I,J_F^{-1},K} \quad (2.15)$$

$$(\dot{s}_3)^{N^1}_{I^{\frac{1}{2}},J_F,K^{\frac{1}{2}}} = (v_3)^{N^1}_{I^{\frac{1}{2}},J_F^1,K^{\frac{1}{2}}} - (v_3)^{N^1}_{I^{\frac{1}{2}},J_F^{-1},K^{\frac{1}{2}}}. \quad (2.16)$$

On the contrary, thin layer method requires only shear traction components directly at the fault plane and shear velocity components at the velocity plane shifted by  $\Delta h/2$ . Thin zone thickness is  $\Delta h$ .

Improved thin zone method is acquired by several changes. Fault plane cuts the grid in a stress plane and  $T_1 = \sigma_{12}$  and  $T_3 = \sigma_{23}$  on this plane are taken as trial traction components. Two velocity planes  $(J_F - 1/2)$  and  $(J_F + 1/2)$

directly next to the fault plane contain the shear velocity components for the calculation of the slip rate and together they create an inelastic zone of thickness  $\Delta h$ . The whole procedure is then very similar as in the case of the thick zone – the trial traction is calculated, the fault condition is applied, modifying the value of traction, followed by the calculation of the velocity and the slip rate.

## 2.3 Traction at split node method

In this section, the traction at split node implementation of the fault boundary condition is introduced independently of a chosen FD grid – the values are expected to be all in a single node. The concrete application, using specific staggered grid scheme, is then described in the second half of this section.

It was developed independently by Andrews [1973] and Day [1977] and used in combination with partially staggered grid FD method in the first case and finite element method in the second case. Description of its use with staggered grid was given by Dalguer and Day [2007], which is followed closely in the second half of this section.

The fault plane cuts through the domain, dividing it into two half spaces '+' and '-'. Every node on the fault plane belongs to both halfspaces + and -. To obtain the complete partition into the two halfspaces, these nodes are cut into two split nodes, with their distinct masses, velocities, stresses and material properties. The only quantity they share is traction  $T_i$ . The mass of the split node is calculated as  $M^\pm = \Delta h^3 \rho^\pm / 2$  in the case of fault cutting the split node (and its FD 'cube' with side equal to  $\Delta h$ ) in half (Fig 2.3).

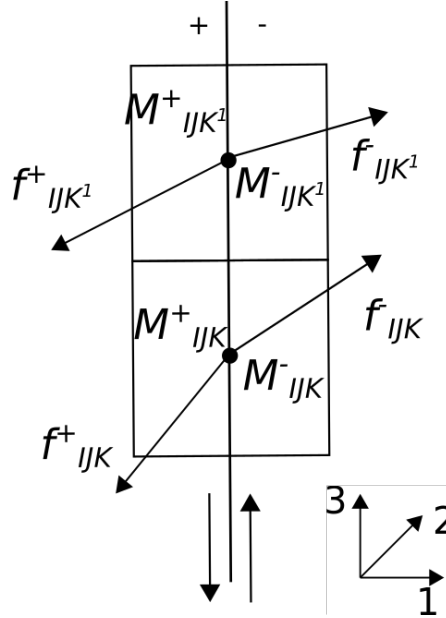


Figure 2.3: Illustration of the split node. Both FD grid nodes at positions given by indexes  $IJK$  and  $IJK^1$  are split into two halves denoted as + and -. Halfspace acts upon a split node of mass  $M$  with a force  $f$ .

In both halfspaces, the elastodynamic force acts upon the split nodes and is

equal to the right hand side of the elastodynamic equation (1.4):

$$f_i^\pm = \frac{1}{\rho^\pm} \sigma_{ij,j}. \quad (2.17)$$

The formula (2.17) represents the body force of the halfspace, without the surface (fault) force – for the calculation of this force, the fault is considered to be a free surface.

Split nodes are coupled through the traction  $T_i$  that generates the surface force  $f_i^c$ . This force is of the same magnitude for both split nodes, but of different orientation. For – side it yields:

$$f_i^c = \Delta h^2 (T_i - T_i^0), \quad (2.18)$$

where  $T_i^0$  is a traction at the initial state of equilibrium.

The acceleration in split nodes can be written from the 2nd Newton's law:

$$\frac{\partial v_i^\pm}{\partial t} = (f_i^\pm \mp f_i^c) / M^\pm. \quad (2.19)$$

It is introduced into the FD formulas as the right hand side of the updating scheme for the velocity components at the fault plane:

$$(v_i^\pm)^{N1} = (v_i^\pm)^N + \Delta t \left[ (f_i^\pm)^{N\frac{1}{2}} \mp \Delta h^2 \left( (T_i)^{N\frac{1}{2}} - T_i^0 \right) \right] / M^\pm, \quad (2.20)$$

Slip rate is calculated from (2.2), as a difference between the velocity values in both split nodes:

$$(\dot{s}_i)^{N1} = (\dot{s}_i)^N + \Delta t \left[ \frac{(f_i^+)^{N\frac{1}{2}}}{M^+} - \frac{(f_i^-)^{N\frac{1}{2}}}{M^-} + \frac{(T_i)^{N\frac{1}{2}} - T_i^0}{\Delta h^{-2} M^-} - \frac{(T_i)^{N\frac{1}{2}} - T_i^0}{\Delta h^{-2} M^+} \right], \quad (2.21)$$

which can be rearranged to:

$$(\dot{s}_i)^{N1} = (\dot{s}_i)^N + \frac{\Delta t (M^- + M^+)}{\Delta h^{-2} M^- M^+} \left[ \frac{M^- (f_i^+)^{N\frac{1}{2}} - M^+ (f_i^-)^{N\frac{1}{2}}}{\Delta h^2 (M^- + M^+)} + (T_i)^{N\frac{1}{2}} - T_i^0 \right]. \quad (2.22)$$

Next we can distinguish between two cases: with zero and with non zero slip rate  $(\dot{s}_i)^{N1}$ . The traction in the former case is a trial traction and again denoted as  $T_i^T$ . We can simply express it from equation (2.22) considering  $(\dot{s}_i)^{N1} = 0$ :

$$(T_i^T)^{N\frac{1}{2}} = T_i^0 + \frac{\Delta t^{-1} M^- M^+ (\dot{s}_i)^N + M^- (f_i^+)^{N\frac{1}{2}} - M^+ (f_i^-)^{N\frac{1}{2}}}{\Delta h^2 (M^- + M^+)}. \quad (2.23)$$

This result is working even for faults that are neither vertical nor planar. From here, we will again continue with only vertical planar faults in the 13 plane. It means, that calculated trial traction has a normal component  $(T_2^T)^{N\frac{1}{2}}$  and two shear components  $(T_1^T)^{N\frac{1}{2}}$  and  $(T_3^T)^{N\frac{1}{2}}$ .

When the value of trial shear traction  $(T_i^T)^{N\frac{1}{2}}$  is higher then frictional force  $S^{N\frac{1}{2}}$ , faulting occurs and  $(\dot{s})^{n1} \neq 0$ . Conditions (2.3) and (2.4) need to be enforced. What is the difference between the trial traction and the traction in the

case when the fault is slipping? It can be acquired by subtracting (2.22) in the first case ( $\dot{s}^{N^1} = 0, (T_i)^{N^{\frac{1}{2}}} = (T_i^T)^{N^{\frac{1}{2}}}$ ) from the same equation in the second case ( $\dot{s}^{N^1} \neq 0$ ), which leads to

$$(\dot{s}_i)^{N^1} = \Delta t \frac{\Delta h^2 (M^- + M^+)}{M^- M^+} \left( (T_i)^{N^{\frac{1}{2}}} - (T_i^T)^{N^{\frac{1}{2}}} \right). \quad (2.24)$$

The time discretization of the used formulas led to the traction being calculated at time  $(N + \frac{1}{2})\Delta t$ , while the slip rate is acquired at the time  $(N + 1)\Delta t$ . However, these quantities are both needed in the colinearity condition (2.6). Evaluation of both quantities at one time requires interpolation, which can cause unwanted oscillations. Values at different times are therefore used:

$$(T_i)^{N^{\frac{1}{2}}} \dot{s}^{N^1} - S^{N^{\frac{1}{2}}} (\dot{s}_i)^{N^1} = 0, \quad (2.25)$$

and inserting (2.24) substituted for  $(\dot{s}_i)^{N^1}$  in 2.25 yields:

$$\left( S^{N^{\frac{1}{2}}} + (\Delta T)^{N^{\frac{1}{2}}} \right) (T_i)^{N^{\frac{1}{2}}} = S^{N^{\frac{1}{2}}} (T_i^T)^{N^{\frac{1}{2}}}. \quad (2.26)$$

Here  $(\Delta T)^{N^{\frac{1}{2}}}$  is the absolute value of the difference between the shear traction and the shear trial traction. This formula ties value of  $(T_i)^{N^{\frac{1}{2}}}$  with frictional force  $S^{N^{\frac{1}{2}}}$ . Solution to equation (2.26),

$$(T_i)^{N^{\frac{1}{2}}} = S^{N^{\frac{1}{2}}} \frac{(T_i^T)^{N^{\frac{1}{2}}}}{(T^T)^{N^{\frac{1}{2}}}}, \quad (2.27)$$

also fulfills the condition (2.3).

The final formula for shear traction is:

$$(T_i)^{N^{\frac{1}{2}}} = \begin{cases} (T_i^T)^{N^{\frac{1}{2}}}, & \text{if } (T^T)^{N^{\frac{1}{2}}} \leq S^{N^{\frac{1}{2}}} \\ S^{N^{\frac{1}{2}}} \frac{(T_i^T)^{N^{\frac{1}{2}}}}{(T^T)^{N^{\frac{1}{2}}}}, & \text{if } (T^T)^{N^{\frac{1}{2}}} > S^{N^{\frac{1}{2}}}, \end{cases} \quad i = 1, 3. \quad (2.28)$$

Normal value of traction is not changing. This formula is formally the same as in the case of the thick/thin layer methods (2.14). The major difference is that the trial traction is calculated in the same node as the slip rate. Traction at split node approach was typically utilized in combination with finite differences with partly staggered grid, whose advantage is the calculation of all components of stress or velocity at one point. Use of the staggered grid leads to certain complications, caused by the staggered position of the individual stress and velocity components [Dalguer and Day, 2007].

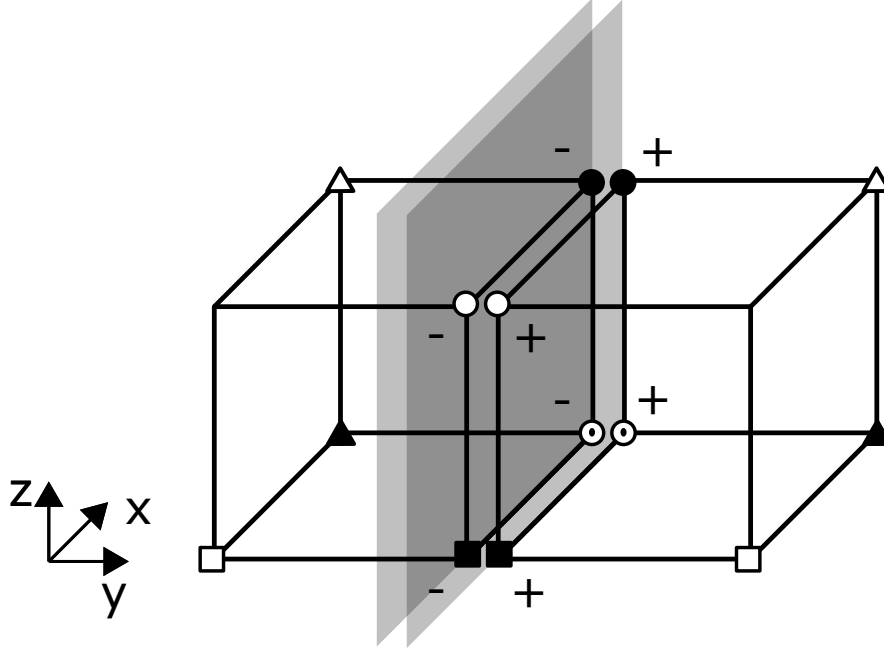


Figure 2.4: Fault plane dividing the FD staggered grid, when traction at split node method is applied. Discontinuous components calculated directly at the fault plane have their + and - value in the same node.

The first of them is again the calculation of the value of the trial traction – the interpolation or further simplification of the faulting model to a plain strike slip or dip slip is needed. All components directly at the fault need to be calculated using the modified FD formulas, which take into account the division of the space by the fault boundary. The exception is  $\sigma_{13}$ , that doesn't require knowledge of any velocity components on the other side of the fault. Discontinuous  $\sigma_{13}^\pm$  can be therefore acquired on both sides using the second or forth order FD formulas.

The shear velocity components  $(v_1^\pm)_{I,J_F,K}$  and  $(v_3^\pm)_{I^{\frac{1}{2}},J_F,K^{\frac{1}{2}}}$  will be calculated from (2.20). Index  $J_F$  denotes components directly at the fault. The elastodynamic forces at the fault  $(f_1^\pm)_{I,K}$  and  $(f_3^\pm)_{I^{\frac{1}{2}},K^{\frac{1}{2}}}$  need to be calculated using second order FD along 1 and 3 axes, but only one-sided FD along the 3 axis. For the purpose of the body force calculation, the traction components  $\sigma_{12}, \sigma_{23}$  are considered zero at the boundary:

$$(f_1^\pm)_{I,K} = \Delta h^2 \left[ (D_1^{(2)} \sigma_{11}^\pm)_{I,J_F,K} + (D_3^{(2)} \sigma_{13}^\pm)_{I,J_F,K} \pm (\sigma_{12})_{I,J_F^{\pm\frac{1}{2}},K} \right] \quad (2.29)$$

$$(f_3^\pm)_{I^{\frac{1}{2}},K^{\frac{1}{2}}} = \Delta h^2 \left[ (D_1^{(2)} \sigma_{13}^\pm)_{I^{\frac{1}{2}},J_F,K^{\frac{1}{2}}} + (D_3^{(2)} \sigma_{33}^\pm)_{I^{\frac{1}{2}},J_F,K^{\frac{1}{2}}} \pm (\sigma_{23})_{I^{\frac{1}{2}},J_F^{\pm\frac{1}{2}},K^{\frac{1}{2}}} \right] \quad (2.30)$$

Normal stress component  $\sigma_{22}$  is continuous at the fault, while  $\sigma_{11}$  and  $\sigma_{33}$  are not. They all require partial derivative of  $v_2$  along the axis 3. The central difference formula is again switched to the one-sided one. The value  $(v_2)_{I^{\frac{1}{2}},J_F,K}$  is acquired from the condition on continuous  $\sigma_{22}$  and  $v_2$ . Equating formulas for its

plus and minus sides leads to (for spatially constant  $\lambda$  and  $\mu$ )

$$\begin{aligned} \frac{4(\lambda + 2\mu)}{\Delta h} (v_2)_{I^{\frac{1}{2}}, J_F, K} &= \frac{2(\lambda + 2\mu)}{\Delta h} \left[ (v_2)_{I^{\frac{1}{2}}, J_F^{-\frac{1}{2}}, K} + (v_2)_{I^{\frac{1}{2}}, J_F^{\frac{1}{2}}, K} \right] \\ &+ \frac{\lambda}{\Delta h} \left[ -(D_1^{(2)} v_1^-)_{I^{\frac{1}{2}}, J_F, K} - (D_3^{(2)} v_3^-)_{I^{\frac{1}{2}}, J_F, K} + (D_1^{(2)} v_1^+)_{I^{\frac{1}{2}}, J_F, K} + (D_3^{(2)} v_3^+)_{I^{\frac{1}{2}}, J_F, K} \right]. \end{aligned} \quad (2.31)$$

One sided difference of  $v_2$  is used to calculate the rest of the stress components at the fault:

$$\begin{aligned} \frac{(\sigma_{11}^{\pm})_{I^{\frac{1}{2}}, J_F, K}^{N^{\frac{1}{2}}} - (\sigma_{11}^{\pm})_{I^{\frac{1}{2}}, J_F, K}^{N^{-\frac{1}{2}}}}{\Delta t} &= (\lambda + 2\mu) (D_1^{(2)} v_1^{\pm})_{I^{\frac{1}{2}}, J_F, K}^N \\ &+ \lambda (D_3^{(2)} v_3^{\pm})_{I^{\frac{1}{2}}, J_F, K}^N \pm \lambda \frac{(v_2)_{I^{\frac{1}{2}}, J_F, K}^N - (v_2)_{I^{\frac{1}{2}}, J_F, K}^N}{\Delta h/2}, \end{aligned} \quad (2.32)$$

$$\begin{aligned} \frac{(\sigma_{22})_{I^{\frac{1}{2}}, J_F, K}^{N^{\frac{1}{2}}} - (\sigma_{22})_{I^{\frac{1}{2}}, J_F, K}^{N^{-\frac{1}{2}}}}{\Delta t} &= \lambda (D_1^{(2)} v_1^{\pm})_{I^{\frac{1}{2}}, J_F, K}^N \\ &+ \lambda (D_3^{(2)} v_3^{\pm})_{I^{\frac{1}{2}}, J_F, K}^N \pm (\lambda + 2\mu) \frac{(v_2)_{I^{\frac{1}{2}}, J_F, K}^N - (v_2)_{I^{\frac{1}{2}}, J_F, K}^N}{\Delta h/2}, \end{aligned} \quad (2.33)$$

$$\begin{aligned} \frac{(\sigma_{33}^{\pm})_{I^{\frac{1}{2}}, J_F, K}^{N^{\frac{1}{2}}} - (\sigma_{33}^{\pm})_{I^{\frac{1}{2}}, J_F, K}^{N^{-\frac{1}{2}}}}{\Delta t} &= \lambda (D_1^{(2)} v_1^{\pm})_{I^{\frac{1}{2}}, J_F, K}^N \\ &+ (\lambda + 2\mu) (D_3^{(2)} v_3^{\pm})_{I^{\frac{1}{2}}, J_F, K}^N \pm \lambda \frac{(v_2)_{I^{\frac{1}{2}}, J_F, K}^N - (v_2)_{I^{\frac{1}{2}}, J_F, K}^N}{\Delta h/2}. \end{aligned} \quad (2.34)$$

The use of the second order FD formulas causes unwanted high frequency oscillations. Dalguer and Day [2007] uses artificial viscous damping of force  $f_i^{\pm}$  to suppress them. Damped force

$$\dot{f}_i^{\pm} = f_i^{\pm} + \eta \dot{f}_i^{\pm} \quad (2.35)$$

is used to calculate shear velocity components at the fault. Damping coefficient  $\eta$  depends on the time discretization parameter  $\eta = \eta_s \Delta t$ , with ideal value of  $\eta_s$  being 0.3. This value was determined experimentally to have the lowest impact on rupture velocity speed by Dalguer and Day [2007]. Dependence on  $\Delta t$  ties damping also to the space discretization (through CFL criterium) and damps frequencies close to the grid Nyquist limit.

## 2.4 Slip weakening friction

Slip weakening friction law was first introduced by Ida [1973], and is extensively used in dynamic rupture simulations. Value of the frictional coefficient depends only on slip

$$S = \sigma_n \mu_f(s). \quad (2.36)$$

For the rupture to propagate, the frictional force needs to decrease with continual sliding (slip weakening). We consider linear slip weakening relationship in the form introduced by Andrews [1976]:

$$\mu_f(s) = \begin{cases} \mu_s - (\mu_s - \mu_d)s/D_c, & \text{if } s < D_c \\ \mu_d, & \text{if } s \geq D_c, \end{cases} \quad (2.37)$$

where  $\mu_s, \mu_d$  and  $D_c$  are model parameters: Static friction coefficient  $\mu_s$  is a value of friction at the beginning of the sliding, friction then linearly drops to the dynamic friction  $\mu_d < \mu_s$  over the slip interval of  $D_c$  as can be seen in Fig (2.5).

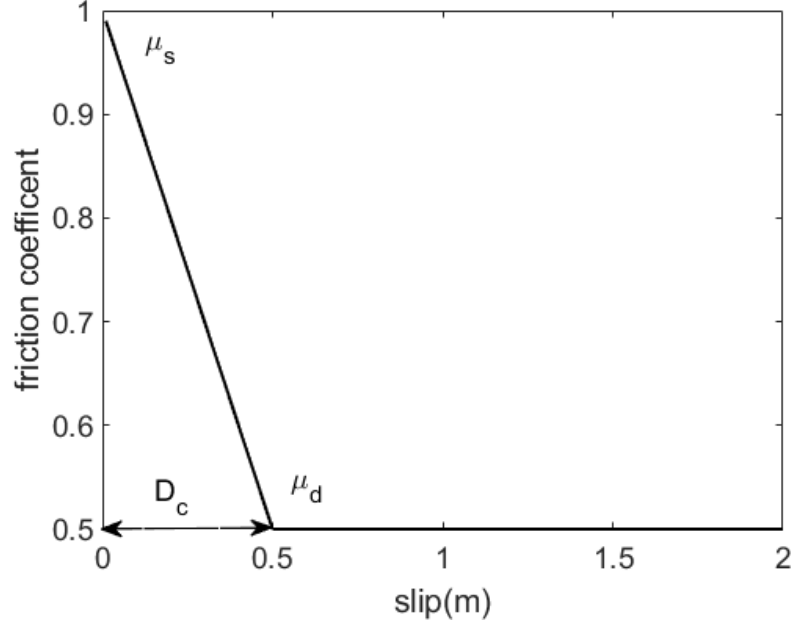


Figure 2.5: Slip weakening friction law (black line) with labeled values of static ( $\mu_s$ ) and dynamic ( $\mu_d$ ) friction coefficients. Critical slip  $D_c$  is marked by arrows.

The calculation of the frictional force during a dynamic rupture simulation requires knowledge of slip at every time level. That is acquired by the integration of the slip rate  $\dot{s}$ . Using the time staggered location of the slip and the slip rate, the integration is straightforward:

$$s^{N\frac{1}{2}} = s^{N-\frac{1}{2}} + \Delta t \dot{s}^N. \quad (2.38)$$

Frictional strength can then be directly calculated at all desired time levels:

$$S^{N\frac{1}{2}} = \begin{cases} \sigma_n [\mu_s - (\mu_s - \mu_d) s^{N\frac{1}{2}} / D_c], & \text{if } s^{N\frac{1}{2}} < D_c \\ \sigma_n \mu_d, & \text{if } s^{N\frac{1}{2}} \geq D_c. \end{cases} \quad (2.39)$$



## 2.5 Rate and state friction with fast velocity weakening

### 2.5.1 The law of friction

Rate and state type laws were developed by Dieterich [1986] and Ruina [1983] based on friction experiments with changing sliding velocity (velocity jump and slide hold slide experiments). Friction depends on a sliding velocity and a state variable  $\psi$

$$S = \sigma_n \mu_f(\dot{s}, \psi). \quad (2.40)$$

The state variable describes the state of the contacts at the surface boundary. Its behaviour follows the slip weakening law with contacts wearing down through sliding,  $\psi$  decreases during the sliding period. In addition to this behavior, increase of the state variable (and friction) during a period of slower sliding is possible, which simulates healing of the fracture. Behavior of the state is described by an evolution law, which is an ordinary differential equation:

$$\frac{d\psi}{dt} = F(s, \dot{s}, \psi). \quad (2.41)$$

Originally, the friction experiments were done at low speeds of the order of millimeters per second [Dieterich, 1979]. Experiments with higher rates became available when rotating disks of studied material were used. Two main effects were observed – frictional instability at medium rates between 1 mm/s and 10 cm/s [Reches and Lockner, 2010] and rapid decrease of the friction at rates above 10 cm/s [Di Toro et al., 2004, Goldsby and Tullis, 2011]. The first effect is attributed to the lubrication of the fault by spontaneous development of the gauge created at the frictional surface [Reches and Lockner, 2010]. The second effect is important for the rupture dynamics, since it occurs at slip rates observed typically during earthquakes. Flash heating of asperities (contacts) was suggested as a probable mechanism. The lifetime of the asperity was compared with time needed to weaken it through heating under a given velocity [Rice, 2006]. When the slip velocity is higher then weakening velocity  $\dot{s}_w$ , the asperity is weakened, when lower, it is not.

Unlike the slip weakening law, the rate and state type laws often do not allow for the surface to stop sliding ( $\dot{s} = 0$ ). The whole fault is considered to be sliding, at initial non-zero slip rate  $\dot{s}_{ini}$ . This value is added rather as a regularization, it does not necessarily have a physical meaning. The traction is set to be always equal to the frictional strength, meaning that only the second case in (2.5) applies.

Several versions of the fast velocity weakening law are employed in the literature [Dunham et al., 2011, Gabriel et al., 2012]. We use the version used by Harris et al. [2018] because its use in their benchmark exercise will allow us to easily estimate the accuracy of the developed code. It consists of five interlinked

formulas:

$$\begin{aligned}
S &= \sigma_n a \operatorname{arcsinh} \left[ \frac{\dot{s}}{2\dot{s}_0} \exp \left( \frac{\psi}{a} \right) \right], \\
\frac{d\psi}{dt} &= -\frac{\dot{s}}{L} [\psi - \psi_{SS}], \\
\psi_{SS} &= a \log \left[ \frac{2\dot{s}_0}{\dot{s}} \sinh \left( \frac{f_{SS}}{a} \right) \right], \\
f_{SS} &= f_w + \frac{f_{LV} - f_w}{[1 + (\dot{s}/\dot{s}_w)^8]^{1/8}}, \\
f_{LV} &= f_0 - (b - a) \log \left( \frac{\dot{s}}{\dot{s}_0} \right).
\end{aligned} \tag{2.42}$$

When constant sliding velocity  $\dot{s}$  is set and held for a sufficiently long time, the system develops into a steady state. The state variable  $\psi$  has its steady state value  $\psi_{SS}$  and frictional strength equals:

$$\begin{aligned}
S_{SS} &= \sigma_n f_{SS}(\dot{s}), \\
f_{SS}(\dot{s}) &= f_w + \frac{f_{LV}(\dot{s}) - f_w}{[1 + (\dot{s}/\dot{s}_w)^8]^{1/8}}, \\
f_{LV}(\dot{s}) &= f_0 - (b - a) \log \left( \frac{\dot{s}}{\dot{s}_0} \right).
\end{aligned} \tag{2.43}$$

Behavior in this steady state is explored first. For low values of  $\dot{s}$ , the steady state friction coefficient is basically equal to  $f_{LV}$  ('Low Velocity'). The development of friction for increasing (but still small)  $\dot{s}$  depends on the sign of  $(b - a)$ . For  $b > a$  the friction law is velocity weakening and decreases, for  $b < a$  it is velocity strenghtening. When  $\dot{s} = \dot{s}_0$ ,  $f_{SS} = f_0$ . For very high values of  $\dot{s}$  the friction coefficient drops to its minimal value  $f_w$  as  $\sim 1/\dot{s}$ .

The time dependent behavior of the friction for changing  $\dot{s}$  is controlled by a differential equation for the state variable (2.42). The solution of the equation for the case of the velocity jump from one constant value to another is an exponential increase or decrease of the state variable towards the steady state value:

$$\psi(t) = [\psi(t_0) - \psi_{SS}(\dot{s})] \exp \left( -\frac{\dot{s}t}{L} \right) + \psi_{SS}(\dot{s}), \tag{2.44}$$

where  $\psi(t_0)$  is the state variable value before the velocity jump,  $\dot{s}$  is the new sliding velocity and  $\psi_{SS}$  the new steady state value. Time scale for this change is  $L/\dot{s}$ . In the case when the new velocity becomes smaller, the friction increases at the same time scale – the fault starts to heal. The development of friction for different velocities is shown in Fig 2.6.

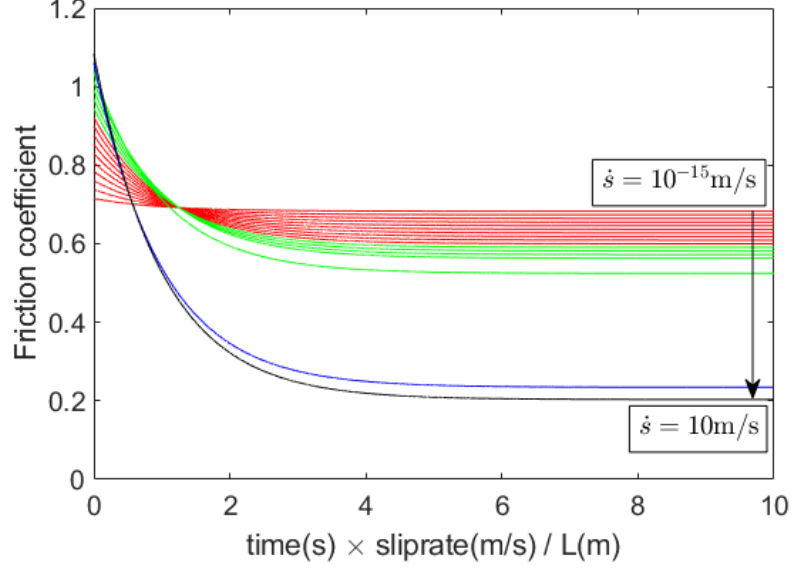


Figure 2.6: The development of friction coefficient after a velocity jump from  $\dot{s}_{ini} = 10^{-16}$  to a higher velocity. Every line shows the development for the different velocity taken from the interval  $10^{-15}$  m/s to 10 m/s. The distribution of velocities is logarithmic ( $10^{-15}, 10^{-14}, \dots$ ). Lines are colour-coded – red (from  $10^{-15}$  m/s to  $10^{-6}$  m/s =  $\dot{s}_0$ ), green (from  $10^{-5}$  m/s to  $10^{-2}$  m/s =  $\dot{s}_w$ ), blue (1 m/s) and black (10 m/s). Friction parameters are in this case  $f_0 = 0.6$  and  $f_w = 0.2$ .

### 2.5.2 Numerical implementation

Rupture simulation with the rate and state friction is more complicated than in the slip weakening case. It requires the solution of two coupled differential equations at the fault boundary – one for the shear velocity components (slip rate) and the other for the state variable  $\psi$ . The traction at split node method contains discretized formula for the slip rate based on the Newton's law (2.24). The second equation is the evolution law for the state variable. In the case of the fast velocity weakening friction from (2.42):

$$\frac{d\psi}{dt} = -\frac{\dot{s}}{L}[\psi - \psi_{ss}(\dot{s})] \quad (2.45)$$

The following approach to numerical discretization and solution of the velocity-state system of differential equations is adopted from Rojas et al. [2009]. Concrete procedure of solving this set of equations depends on the distribution of velocity and state variable between time levels. For the time staggered schemes, such as the scheme used in this work, the time-staggered distribution of slip rate and state variable (as in the Fig 2.7) is natural. The results are similarly accurate as using unstaggered distribution with high-order Rosenbrock integration [Rojas et al., 2009], while the coding is simpler.

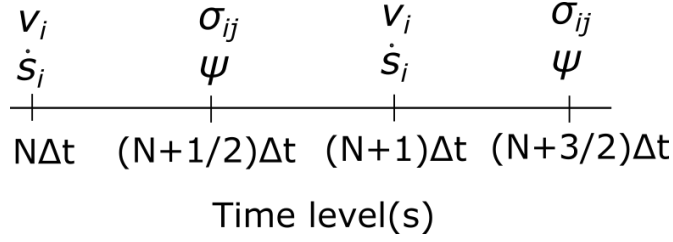


Figure 2.7: The time staggered position of slip rate and state variable

First step is the integration of the evolution law for  $\psi$  in the interval between two successive time levels  $(N-1/2)\Delta t$  and  $(N+1/2)\Delta t$ . Due to the time-staggered distribution, slip rate is positioned in the middle of this interval  $N\Delta t$ , and it will be approximated by this value over the whole interval  $\dot{s}(t) = (\dot{s})^N, \forall t \in ((N-1/2)\Delta t, (N+1/2)\Delta t)$ . With the slip rate constant over the whole interval, the solution of the differential equation (2.44) applies:

$$\begin{aligned}
 \psi^{N\frac{1}{2}} &= (\psi^{N-\frac{1}{2}} - \psi_{SS}(\dot{s}^N)) \exp\left(-\frac{\dot{s}^N \Delta t}{L}\right) + \psi_{SS}(\dot{s}^N), \\
 \psi_{SS}(\dot{s}^N) &= a \log \left[ \frac{2s_0}{\dot{s}^N} \sinh\left(\frac{f_{SS}(\dot{s}^N)}{a}\right) \right], \\
 f_{SS}(\dot{s}^N) &= f_w + \frac{f_{LV}(\dot{s}^N) - f_w}{\left[1 + (\dot{s}^N/s_w)^8\right]^{1/8}}, \\
 f_{LV}(\dot{s}^N) &= f_0 - (b-a) \log\left(\frac{\dot{s}^N}{s_0}\right).
 \end{aligned} \tag{2.46}$$

Second step is the calculation of slip rate  $(\dot{s})^{N^1}$  from (2.22). Slipping will be allowed only in the direction of one shear component. Equation for the slip rate is therefore considered in scalar form:

$$(\dot{s})^{N^1} = (\dot{s})^N + \frac{\Delta t(M^- + M^+)}{\Delta h^{-2}M^-M^+} \left( \frac{M^-(f^+)^{N\frac{1}{2}} - M^+(f^-)^{N\frac{1}{2}}}{\Delta h^2(M^- + M^+)} + (T)^{N\frac{1}{2}} - T^0 \right). \tag{2.47}$$

Since the fault is considered to be always sliding, the second case from (2.28) will be directly substituted into (2.47) for traction and the first equation from (2.42) as the friction  $S$ :

$$(\dot{s})^{N^1} = (\dot{s})^N + \frac{\Delta t(M^- + M^+)}{\Delta h^{-2}M^-M^+} \left( \frac{M^-(f^+)^{N\frac{1}{2}} - M^+(f^-)^{N\frac{1}{2}}}{\Delta h^2(M^- + M^+)} + S(\dot{s}^?, \psi^{N\frac{1}{2}}) - T^0 \right). \tag{2.48}$$

Slip rate  $\dot{s}^?$  on the right hand side of (2.48) cannot be set as a value of slip rate in the previous time level  $\dot{s}^? = (\dot{s})^N$  (Forward Euler method), because the resulting scheme is highly unstable, especially for small values of slip rate, where the derivative of  $\text{arcsinh}(x)$  has its highest value. Backward Euler scheme ( $\dot{s}^? = \dot{s}^{N^1}$ ) or trapezoidal scheme ( $\dot{s}^? = (\dot{s}^N + \dot{s}^{N^1})/2$ ) needs to be used instead. Although trapezoidal scheme offers higher order accuracy, in reality it does not make much improvement. Backward Euler scheme will be used in this chapter, yielding

$$(\dot{s})^{N^1} = (\tilde{s})^N + C \text{arcsinh}\left[\frac{(\dot{s})^{N^1}}{2s_0} \exp\left(\frac{\psi^{N\frac{1}{2}}}{a}\right)\right], \tag{2.49}$$

where

$$(\tilde{s})^N = (\dot{s})^N + \frac{\Delta t(M^- + M^+)}{\Delta h^{-2}M^-M^+} \left( \frac{M^-(f^+)^{N^{\frac{1}{2}}} - M^+(f^-)^{N^{\frac{1}{2}}}}{\Delta h^2(M^- + M^+)} - T^0 \right) \quad (2.50)$$

denotes the part of the formula (2.47) already explicitly calculated before the time level  $(n+1)\Delta t$ , and

$$C = \frac{\Delta t(M^- + M^+)}{\Delta h^{-2}M^-M^+} \sigma_n a. \quad (2.51)$$

Formula (2.49) is nonlinear and needs to be solved accordingly, for example with the Newton's method, which will be described next.

We want to find a new slip rate value  $(\dot{s})^{N^1}$ , that satisfies equation (2.49). This is equivalent to finding a root of a function

$$F((\dot{s})^{N^1}) = (\tilde{s})^N - (\dot{s})^{N^1} + C \operatorname{arcsinh} \left[ \frac{(\dot{s})^{N^1}}{2s_0} \exp \left( \frac{\psi^{N^{\frac{1}{2}}}}{a} \right) \right]. \quad (2.52)$$

In Newton's method the root  $w$  of the function  $F(x)$ , is found approximately by a successive iteration:

$$w_{n+1} = w_n - \frac{F(w_n)}{F'(w_n)}, \quad (2.53)$$

where  $F'$  is the derivative of function  $F$ , and  $w_n$  is the approximate value of the root at the  $n$ -th iteration. Equation (2.49) is modified to simplify finding the solution. Solution is found for a substituted variable:

$$w = \operatorname{arcsinh} \left[ \frac{(\dot{s})^{N^1}}{2s_0} \exp \left( \frac{\psi^{N^{\frac{1}{2}}}}{a} \right) \right] \quad (2.54)$$

instead of slip rate. This leads to a simple form of the function:

$$F(w) = (\tilde{s})^N + Cw - \exp \left( \frac{-\psi^{N^{\frac{1}{2}}}}{a} \right) 2s_0 \sinh(w), \quad (2.55)$$

allowing to simply find its derivative:

$$F'(w) = C - \exp \left( \frac{-\psi^{N^{\frac{1}{2}}}}{a} \right) 2s_0 \cosh(w). \quad (2.56)$$

Natural choice of the starting value of  $w$  is its value at the previous time level:

$$w_0 = \operatorname{arcsinh} \left[ \frac{(\dot{s})^N}{2s_0} \exp \left( \frac{\psi^{N^{\frac{1}{2}}}}{a} \right) \right]. \quad (2.57)$$

Formula (2.53) is then applied iteratively until the difference between successive values of  $w$  (the error of the approximation) is lower than a chosen value – in our implementation  $10^{-5}$  for a single precision calculation and  $10^{-8}$  for a double precision one. The value of slip rate solving (2.49) is calculated from the substitution (2.54):

$$(\dot{s})^{N^1} = \frac{2s_0 \sinh(w)}{\exp \left( \frac{\psi^{N^{\frac{1}{2}}}}{a} \right)}. \quad (2.58)$$

The discrete solution of the fault boundary conditions with the fast velocity weakening rate and state law using the traction at split node method consists of application of formulas (2.46) to acquire new value of the state variable and Newton's method solution of (2.49) to acquire the new value of the slip rate. This is done at every node at the fault surface independently.

## 2.6 Cohesive zone

The part of the fault behind the crack-tip, where the traction drops from its static to its dynamic value, is called cohesive (or process) zone  $\Lambda$ . The resolution of the cohesive zone (amount of discrete points per cohesive zone) is the main parameter controlling the accuracy of the numerical simulation [Dalgner and Day, 2006]. Indeed, the cohesive zone is the part of the fault, where the nonlinear boundary condition on stress (2.5) is enforced, and where changes in tractions and slip rates are very sharp.

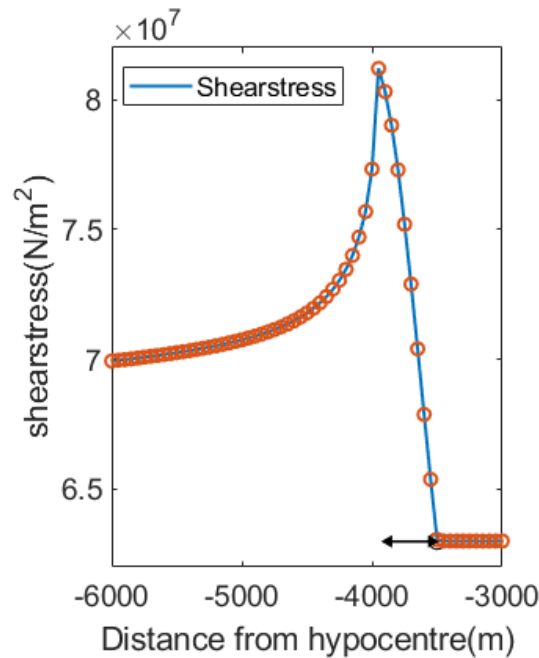


Figure 2.8: Cohesive zone behind a crack-tip – snapshot of spatial dependence of the shear stress for the linear slip weakening law. Arrow defines the cohesive zone. Red circles are values of the traction at discrete points.

Figure (2.8) shows an example of the spatial dependence of the traction in the rupture propagation, illustrating the importance of the proper resolution of the cohesive zone. The discretization in this particular case was  $\Delta h = 50\text{m}$ ; with lower resolution (higher  $\Delta h$ ), the accuracy would drop considerably. Slip rate and traction behind the crack-tip vary quickly also in time. However, the situation is much better here, because the CFL criterion ensures that the time resolution of the 'cohesive time interval' will be much better resolved (see Fig 2.9 for temporal discretization of traction).

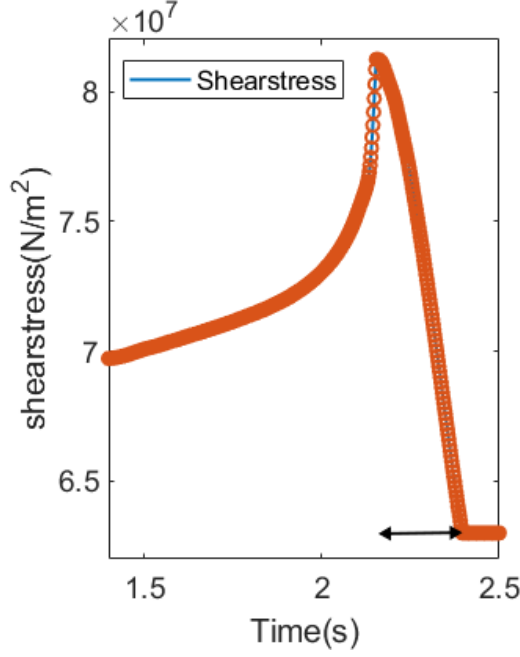


Figure 2.9: The same as in Fig 2.8, but for the temporal discretization.

Having the knowledge of the cohesive zone size before the simulation is run would be useful, because it would allow us to determine the discretization necessary to reach the desired accuracy. However, the dependence of the cohesive zone size on physical parameters of a heterogeneous dynamic model is non-trivial. Several approximated estimations are used [Bizzarri et al., 2012]. Analysis of energy release rate and fracture energy offers an upper bound estimate (for the rupture velocity close to zero) of the cohesive zone size

$$\Lambda_{II}(\mathbf{x}) = \frac{9\pi D_c(\mathbf{x})\mu(\mathbf{x})}{32\sigma_n(\mathbf{x})(\mu_s(\mathbf{x}) - \mu_d(\mathbf{x}))} \quad (2.59)$$

for Mode II and

$$\Lambda_{III}(\mathbf{x}) = \frac{9\pi D_c(\mathbf{x})\mu(\mathbf{x})/(1 - \nu(\mathbf{x}))}{32\sigma_n(\mathbf{x})(\mu_s(\mathbf{x}) - \mu_d(\mathbf{x}))} \quad (2.60)$$

for Mode III cracks ( $\nu$  is Poisson ratio). For non-zero values of the rupture velocity, the cohesive zone will shrink below this estimate, by factors

$$A_{II} = \frac{(1 - \nu)\beta^2 \left( 4(1 - v_r^2/v_\beta^2)^{1/2}(1 - v_r^2/v_\beta^2)^{1/2} - (2 - v_r^2/v_\beta^2)^2 \right)}{v_r^2(1 - v_r^2/v_\beta^2)^{1/2}} \quad (2.61)$$

for a mode II crack and

$$A_{III} = (1 - v_r^2/v_\beta^2)^{1/2}. \quad (2.62)$$

for a mode III crack [Day et al., 2005].

After the simulation, the cohesive zone can be established when knowing the whole field of traction (space and time dependent) by measuring the distance between the maximum and minimum tractions in the direction of the rupture propagation. This approach poses complications when the direction of the rupture propagation changes. In this work we will use the following local estimate of the cohesive zone where the rupture direction and rupture velocity is assumed to not

change locally during the propagation throughout the cohesive zone. For every point at the fault the rupture velocity  $v_r$  is calculated from the eikonal equation as the inverse value of the magnitude of the gradient of the rupture time  $t_r$

$$v_r(\mathbf{x}) = \frac{1}{\sqrt{\left(\frac{\partial t_r(\mathbf{x})}{\partial x_1}\right)^2 + \left(\frac{\partial t_r(\mathbf{x})}{\partial x_2}\right)^2 + \left(\frac{\partial t_r(\mathbf{x})}{\partial x_3}\right)^2}}, \quad (2.63)$$

The cohesive zone is then estimated as

$$\Lambda(\mathbf{x}) = v_r(\mathbf{x}) [t_s(\mathbf{x}) - t_r(\mathbf{x})] \quad (2.64)$$

from the rupture time  $t_r$  (time of maximum traction in the position  $\mathbf{x}$ ) and time  $t_s$  for which the traction is minimal in the position  $\mathbf{x}$ . For the slip weakening friction law,  $t_s$  is also the time in which the value of slip is equal to  $D_c$ .

When the fast velocity weakening friction is assumed, the traction doesn't drop at the same rate over the whole cohesive zone. Majority of the stress drop occurs in a much smaller area behind the crack-tip [Rojas et al., 2009], see Fig. 2.10.

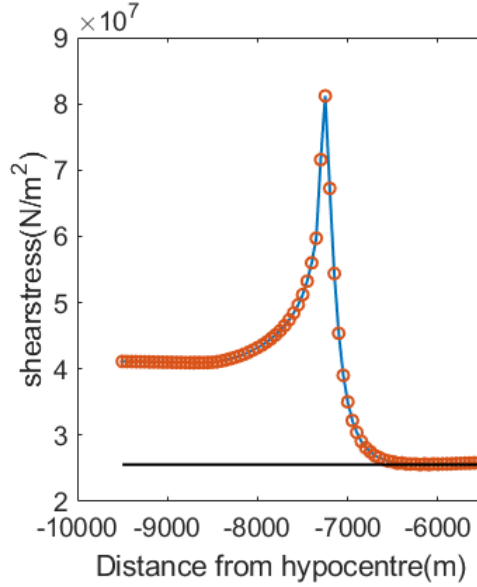


Figure 2.10: Cohesive zone behind a crack-tip – snapshot of spatial dependence of the shear stress for fast velocity weakening friction law. The black line shows the value of minimum traction.

The resolution of this effective cohesive zone is more important for the simulation accuracy. Effective cohesive zone  $\Lambda_e(\mathbf{x})$  is calculated in this case as

$$\Lambda_e(\mathbf{x}) = v_r(\mathbf{x}) [t_e(\mathbf{x}) - t_r(\mathbf{x})], \quad (2.65)$$

where  $t_e$  is set as a time, where the traction would reach the minimum value if the drop proceeded linearly with the rate equal to the maximum derivative of the traction.



## 3. Outer boundary conditions

At the border of the computational domain the outer boundary conditions are in place. Two types of boundary conditions are described in this chapter – free surface (Section 3.1) and absorbing boundary condition (Section 3.2).

### 3.1 Free surface

The interface between the Earth material and atmosphere will be considered to coincide with the 1-2 plane, where zero traction condition is applied,

$$\sigma_{ij} \Big|_{(z=z_s)} n_j = T_i = (\sigma_{13}, \sigma_{23}, \sigma_{33}) = 0, \quad (3.1)$$

where  $n_j = (0, 0, 1)$  is the normal to the free surface and  $z_s$  is the  $z$  position of the free surface plane.

The spatial differences of the velocity or stress components below and at the free surface are calculated using the 4th order central FD formula. This requires the knowledge of the velocity and stress components at nodes above the free surface. Their values will be set so that condition (3.1) is satisfied at the free surface for all the three components of traction. This is known as a stress imaging method [Graves, 1996]. Alternatives to this approach are to set material parameters  $\rho$ ,  $\lambda$ ,  $\mu$  above the free surface to approach zero (vacuum formulation [Graves, 1996]), or to change the FD formulas near the free surface to one-sided ones (AFDA method [Kristek et al., 2002]), which brings improvement in the modeling of the surface waves over longer distances, but is probably unnecessary for the rupture propagation simulations.

There are two ways in which the free surface (FS) plane can cut through the staggered FD grid – through nodes, where  $\sigma_{33}$  is explicitly calculated, or nodes with  $\sigma_{13}$  and  $\sigma_{23}$ . The first choice is called as the H formulation, while the second as the W formulation [Kristek et al., 2002]. In terms of the accuracy the difference between both formulations is minimal [Gottschämmer and Olsen, 2001]. The W formulation is used in this work – it is more natural choice because of the orientation of the FD grid. The position of the FS plane in our staggered grid is shown in Fig 3.1 together with the positions of the required imaged values above the FS. The position of the nodes directly at the plane on the third axis is  $z_s = K_s \Delta h$ .

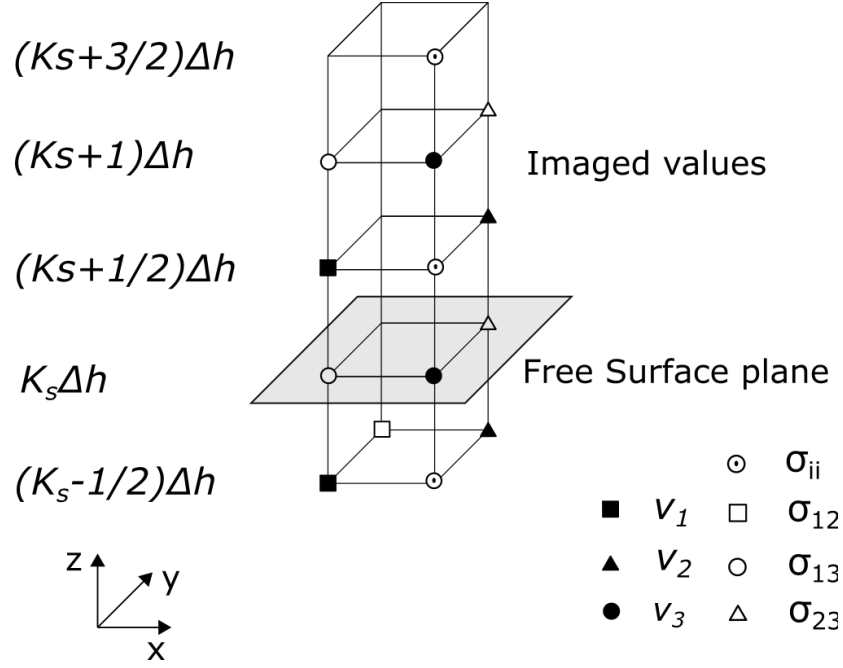


Figure 3.1: Position of the free surface plane in the staggered FD grid in the W formulation. Free surface plane is denoted by a grey plane. Nodes above the plane contain imaged values of the velocity and stress components. Only those imaged values necessary for the calculation are shown.

Both shear components of traction at the free surface are set to zero

$$\begin{aligned} (\sigma_{13})_{IJK_s} &= 0 \\ (\sigma_{23})_{I^{\frac{1}{2}}J^{\frac{1}{2}}K_s} &= 0 \end{aligned} \quad (3.2)$$

and velocity component 3 at the free surface can be calculated using the standard 4th order FD formula. There are 4 stress and 3 velocity values above the free surface required for the central FD formulas on nodes below and at the free surface. All will be set to impose the zero stress condition on traction either directly or for its interpolated value. Imaged values of the stress components 11, 22 and 12 are not needed in this respect.

The normal component of traction  $\sigma_{33}$  is not explicitly calculated at the free surface plane, therefore the value interpolated from two closest points  $(\sigma_{33})_{I^{\frac{1}{2}}JK_s^{\frac{1}{2}}}$  and  $(\sigma_{33})_{I^{\frac{1}{2}}JK_s^{-\frac{1}{2}}}$  is set to zero. This yields antisymmetry of the normal traction component below free surface and the imaged value above:

$$(\sigma_{33})_{I^{\frac{1}{2}}JK_s^{\frac{1}{2}}} = -(\sigma_{33})_{I^{\frac{1}{2}}JK_s^{-\frac{1}{2}}}. \quad (3.3)$$

Similarly, the other imaged values of stress components above the free surface are set antisymmetrically to their values below:

$$\begin{aligned} (\sigma_{13})_{IJK_s^1} &= -(\sigma_{13})_{IJK_s^{-1}} \\ (\sigma_{23})_{I^{\frac{1}{2}}J^{\frac{1}{2}}K_s^1} &= -(\sigma_{23})_{I^{\frac{1}{2}}J^{\frac{1}{2}}K_s^{-1}} \\ (\sigma_{33})_{I^{\frac{1}{2}}JK_s^{\frac{3}{2}}} &= -(\sigma_{33})_{I^{\frac{1}{2}}JK_s^{-\frac{3}{2}}}, \end{aligned} \quad (3.4)$$

which yields average zero value between the node below the surface and the imaged one.

Imaged velocity components are set from second order spatial discretization of time derivated Hooke's law at the free surface. It is written for the component of traction, with the right-hand side set to be zero due to (3.1). Hooke's law for 13 component of traction at the free surface gives:

$$0 = (D_t \sigma_{13})_{IJK_s}^N = \frac{\mu}{\Delta h} \left[ (v_1)_{IJK_s^{\frac{1}{2}}}^N - (v_1)_{IJK_s^{-\frac{1}{2}}}^N + (v_3)_{I^{\frac{1}{2}}JK_s}^N - (v_3)_{I^{-\frac{1}{2}}JK_s}^N \right] \quad (3.5)$$

$$(v_1)_{IJK_s^{\frac{1}{2}}}^N = (v_1)_{IJK_s^{-\frac{1}{2}}}^N - \left[ (v_3)_{I^{\frac{1}{2}}JK_s}^N - (v_3)_{I^{-\frac{1}{2}}JK_s}^N \right]$$

Similarly, for the 23 component of stress at the free surface:

$$0 = (D_t \sigma_{23})_{I^{\frac{1}{2}}J^{\frac{1}{2}}K_s}^N = \frac{\mu}{\Delta h} \left[ (v_2)_{I^{\frac{1}{2}}J^{\frac{1}{2}}K_s^{\frac{1}{2}}}^N - (v_2)_{I^{\frac{1}{2}}J^{\frac{1}{2}}K_s^{-\frac{1}{2}}}^N + (v_3)_{I^{\frac{1}{2}}J^{\frac{1}{2}}K_s}^N - (v_3)_{IJ^{\frac{1}{2}}K_s}^N \right]$$

$$(v_2)_{I^{\frac{1}{2}}J^{\frac{1}{2}}K_s^{\frac{1}{2}}}^N = (v_2)_{I^{\frac{1}{2}}J^{\frac{1}{2}}K_s^{-\frac{1}{2}}}^N - \left[ (v_3)_{I^{\frac{1}{2}}J^{\frac{1}{2}}K_s}^N - (v_3)_{IJ^{\frac{1}{2}}K_s}^N \right] \quad (3.6)$$

The 33 component of stress is not calculated directly at the free surface, but Hooke's law can be written for the time differences of both sides in (3.3),

$$(D_t \sigma_{33})_{I^{\frac{1}{2}}JK_s^{\frac{1}{2}}}^N = \frac{\lambda + 2\mu}{\Delta h} \left[ (v_3)_{I^{\frac{1}{2}}JK_s^1}^N - (v_3)_{I^{\frac{1}{2}}JK_s}^N \right]$$

$$+ \frac{\lambda}{\Delta h} \left[ (v_1)_{I^1JK_s^{\frac{1}{2}}}^N - (v_1)_{IJK_s^{\frac{1}{2}}}^N + (v_2)_{I^{\frac{1}{2}}J^{\frac{1}{2}}K_s^{\frac{1}{2}}}^N - (v_2)_{I^{\frac{1}{2}}J^{-\frac{1}{2}}K_s^{\frac{1}{2}}}^N \right]$$

$$(D_t \sigma_{33})_{I^{\frac{1}{2}}JK_s^{-\frac{1}{2}}}^N = \frac{\lambda + 2\mu}{\Delta h} \left[ (v_3)_{I^{\frac{1}{2}}JK_s}^N - (v_3)_{I^{\frac{1}{2}}JK_s^{-1}}^N \right]$$

$$+ \frac{\lambda}{\Delta h} \left[ (v_1)_{I^1JK_s^{-\frac{1}{2}}}^N - (v_1)_{IJK_s^{-\frac{1}{2}}}^N + (v_2)_{I^{\frac{1}{2}}J^{\frac{1}{2}}K_s^{-\frac{1}{2}}}^N - (v_2)_{I^{\frac{1}{2}}J^{-\frac{1}{2}}K_s^{-\frac{1}{2}}}^N \right] \quad (3.7)$$

After substituting these into the time derivative of (3.3), we can express imaged velocity component 3

$$(v_3)_{I^{\frac{1}{2}}JK_s^1}^N = (v_3)_{I^{\frac{1}{2}}JK_s^{-1}}^N - \frac{\lambda}{\lambda + 2\mu} \left[ (v_1)_{I^1JK_s^{\frac{1}{2}}}^N - (v_1)_{IJK_s^{\frac{1}{2}}}^N \right.$$

$$+ (v_1)_{I^1JK_s^{-\frac{1}{2}}}^N - (v_1)_{IJK_s^{-\frac{1}{2}}}^N + (v_2)_{I^{\frac{1}{2}}J^{\frac{1}{2}}K_s^{\frac{1}{2}}}^N - (v_2)_{I^{\frac{1}{2}}J^{-\frac{1}{2}}K_s^{\frac{1}{2}}}^N$$

$$\left. + (v_2)_{I^{\frac{1}{2}}J^{\frac{1}{2}}K_s^{-\frac{1}{2}}}^N - (v_2)_{I^{\frac{1}{2}}J^{-\frac{1}{2}}K_s^{-\frac{1}{2}}}^N \right] \quad (3.8)$$

Formulae (3.2, 3.4, 3.5, 3.6, 3.8) together constitute the stress imaging free surface method. When applied (with all other components at nodes at and below the free surface calculated using the standard 4th order FD formulas), the zero traction condition at the free surface is imposed.

## 3.2 Absorbing boundary conditions

Absorbing boundary conditions (ABCs) occupy domain borders, where further continuation of the material needs to be simulated. Free propagation of waves without any reflections is modeled at these boundaries. Two major approaches

are used in elastodynamic simulations [Moczo et al., 2007] – constructing the boundary condition from the extrapolation of waves or adding an absorbing layer, where the wave amplitude is gradually decreased.

The extrapolation of waves offers an attractively fast code, when a simple model of the wave is introduced and the extrapolation is performed with low order FD formulas [Clayton and Engquist, 1977]. Improvements in accuracy [Higdon, 1991] typically come at the cost of very complicated equations and more memory demand [Moczo et al., 2007].

Absorbing layers are computationally more demanding, since the FD calculation is required in the added layer of non-zero thickness, i.e. the size of the computational domain increases. The main advantage of this approach is, however, that further improvement in accuracy can be achieved by simply widening the absorbing layer, while the extrapolation methods require direct changes in the code and using formulas of increasing complexity.

In this section the popular version of the absorbing layer approach called Perfectly Matched Layers (PML) is described. It was introduced for electromagnetic waves by [Berenger, 1994]. Here we follow papers by Kristek et al. [2009] and Collino and Tsogka [2001]. The second subsection describes approach calculation of the reflection coefficient of the PML layer, which we use to set the damping profile values.

### 3.2.1 Perfectly matched layers

Without loss of generality, let us assume wave propagation in the  $x_1$  direction. At the border of the computational domain an absorbing layer is introduced, where the wave amplitude decrease by propagation in the  $x_1$  direction is desired. This effect is attained by changing elastodynamic equation(1.4) in the layer as follows. We introduce a complex coordinate  $\tilde{x}_1$  instead of  $x_1$ :

$$\begin{aligned}\rho \frac{\partial v_i}{\partial t} &= \frac{\partial \sigma_{1i}}{\partial \tilde{x}_1} + \frac{\partial \sigma_{ji}}{\partial x_j}, & j \neq 1 \\ \frac{\partial \sigma_{ij}}{\partial t} &= c_{ijk1} \frac{\partial v_k}{\partial \tilde{x}_1} + c_{ijkl} \frac{\partial v_k}{\partial x_l}, & l \neq 1,\end{aligned}\tag{3.9}$$

With relation between  $\tilde{x}_1$  and  $x_1$  defined in frequency domain as

$$\tilde{x}_1 = x_1 - \frac{\iota}{\omega} \int_0^{x_1} d_x(s) ds,\tag{3.10}$$

where 0 is set at the divide between both areas and  $d_x$  is a chosen damping profile (real, non-negative function of  $x_1$ ). Plane wave solution of (3.9) now depends on the complex coordinate:

$$v_j = V_j \exp[-\iota(k_1 \tilde{x}_1 + k_2 x_2 + k_3 x_3 - \omega t)]\tag{3.11}$$

which after resubstituting from [3.10], leads to the desired attenuated solution:

$$v_j = V_j \exp[-\iota(k_1 x_1 + k_2 x_2 + k_3 x_3 - \omega t)] \exp\left[-\frac{k_1}{\omega} \int_0^{x_1} d_x(s) ds\right].\tag{3.12}$$

This solution has same amplitude constants  $V_j$ , wave vector  $k_i = (k_1, k_2, k_3)$  and angular frequency  $\omega$  as (1.8) would have in the same area (with same material parameters), but its amplitude decreases with the distance from  $x_1 = 0$ .

The relation (3.10) is defined in the frequency domain and the simulation is executed with equations in the time domain. Altered version of the elastodynamic equation in the layer is first obtained in the frequency domain by substitution of (3.10) into (3.9). Return into the time domain provides the form for FD discretization.

First, we concentrate on the relationship between the partial derivative with respect to  $x_1$  and with respect to  $\tilde{x}_1$ . It will be defined in the frequency domain for arbitrary function  $\hat{f}(x_1, \omega)$ :

$$\frac{\partial \hat{f}}{\partial x_1} = \frac{\partial \hat{f}}{\partial \tilde{x}_1} \frac{\partial \tilde{x}_1}{\partial x_1} \quad (3.13)$$

The derivative of (3.10) provides

$$\frac{\partial \tilde{x}_1}{\partial x_1} = 1 - \frac{\iota}{\omega} d_x \quad (3.14)$$

and by substituting, we get a formula to be substituted into the frequency domain elastodynamic equation

$$\frac{\partial \hat{f}}{\partial \tilde{x}_1} = \frac{\iota \omega}{\iota \omega + d_x} \frac{\partial \hat{f}}{\partial x_1} \quad (3.15)$$

Sums in equations (3.9) are splitted into two parts. The first part consists of all terms without  $\frac{\partial}{\partial \tilde{x}_1}$ , while the second with. Equations are decomposed accordingly into two parts – tangent part  $\hat{\sigma}_{ij}^\perp, \hat{v}_i^\perp$  and parallel  $\hat{\sigma}_{ij}^\parallel, \hat{v}_i^\parallel$ :

$$\begin{aligned} \rho \iota \omega \hat{v}_i^\parallel &= \frac{\partial \hat{\sigma}_{1i}}{\partial \tilde{x}_1} \\ \rho \iota \omega \hat{v}_i^\perp &= \frac{\partial \hat{\sigma}_{ji}}{\partial x_j} \\ \hat{v}_i &= \hat{v}_i^\parallel + \hat{v}_i^\perp \\ \iota \omega \hat{\sigma}_{ij}^\parallel &= c_{ijk1} \frac{\partial \hat{v}_k}{\partial \tilde{x}_1} \\ \iota \omega \hat{\sigma}_{ij}^\perp &= c_{ijkl} \frac{\partial \hat{v}_k}{\partial x_l}, \quad l \neq 1 \\ \hat{\sigma}_{ij} &= \hat{\sigma}_{ij}^\parallel + \hat{\sigma}_{ij}^\perp \end{aligned} \quad (3.16)$$

where the parallel part means the part, whose evolution depends on the spatial derivative in the direction of attenuation. The tangent parts are not attenuated, and don't need any further changes. The substitution for  $\partial \tilde{x}_1$  from is done in tangent parts:

$$\begin{aligned} \rho \iota \omega \hat{v}_i^\parallel &= \frac{\iota \omega}{\iota \omega + d_x} \frac{\partial \hat{\sigma}_{1i}}{\partial x_1} \\ \iota \omega \hat{\sigma}_{ij}^\parallel &= \frac{\iota \omega}{\iota \omega + d_x} c_{ijk1} \frac{\partial \hat{v}_k}{\partial x_1}, \end{aligned} \quad (3.17)$$

and after simple algebra we get

$$\begin{aligned} \rho(\iota \omega + d_x) \hat{v}_i^\parallel &= \frac{\partial \hat{\sigma}_{1i}}{\partial x_1} \\ (\iota \omega + d_x) \hat{\sigma}_{ij}^\parallel &= c_{ijk1} \frac{\partial \hat{v}_k}{\partial x_1}, \end{aligned} \quad (3.18)$$

which leads to the final form in the time domain:

$$\begin{aligned}
\rho \left( \frac{\partial v_i^{\parallel}}{\partial t} + d_x v_i^{\parallel} \right) &= \frac{\partial \sigma_{1i}}{\partial x_1} \\
\rho \frac{\partial v_i^{\perp}}{\partial t} &= \frac{\partial \sigma_{ji}}{\partial x_j}, \quad j \neq 1 \\
v_i &= v_i^{\parallel} + v_i^{\perp} \\
\frac{\partial \sigma_{ij}^{\parallel}}{\partial t} + d_x \sigma_{ij}^{\parallel} &= c_{ijk1} \frac{\partial v_k}{\partial x_1} \\
\frac{\partial \sigma_{ij}^{\perp}}{\partial t} &= c_{ijkl} \frac{\partial v_k}{\partial x_l}, \quad l \neq 1 \\
\sigma_{ij} &= \sigma_{ij}^{\parallel} + \sigma_{ij}^{\perp},
\end{aligned} \tag{3.19}$$

The discretization of the partial derivatives on the right-hand side of (3.19) can be performed by using the second order (1.13) or fourth order [1.16] finite difference formulas. Second order FD formulas and the interpolation in time looks like:

$$\begin{aligned}
\left( \frac{\partial v_i}{\partial t} \right)^{N^{\frac{1}{2}}} &= \frac{(v_i)^{N^1} - (v_i)^N}{\Delta t} & \left( \frac{\partial \sigma_{ij}}{\partial t} \right)^N &= \frac{(\sigma_{ij})^{N^{\frac{1}{2}}} - (\sigma_{ij})^{N^{-\frac{1}{2}}}}{\Delta t} \\
(v_i)^{N^{\frac{1}{2}}} &= \frac{(v_i)^{N^1} + (v_i)^N}{2} & (\sigma_{ij})^N &= \frac{(\sigma_{ij})^{N^{\frac{1}{2}}} - (\sigma_{ij})^{N^{-\frac{1}{2}}}}{2}.
\end{aligned} \tag{3.20}$$

These lead to the explicit formulas for both the stress and velocity components:

$$\begin{aligned}
(v_i^{\parallel})^{N^1} &= \frac{(v_i^{\parallel})^N (1 - \frac{1}{2} \Delta t d_x) + \frac{1}{\rho} D_1^{(2)} (\sigma_{i1})^{N^{\frac{1}{2}}}}{1 + \frac{1}{2} \Delta t d_x} \\
(v_i^{\perp})^{N^1} &= (v_i^{\perp})^N + \frac{1}{\rho} \left[ D_2^{(2)} (\sigma_{i2})^{N^{\frac{1}{2}}} + D_3^{(2)} (\sigma_{i3})^{N^{\frac{1}{2}}} \right] \\
(v_i)^{N^1} &= (v_i^{\parallel})^{N^1} + (v_i^{\perp})^{N^1} \\
(\sigma_{ji}^{\parallel})^{N^{\frac{1}{2}}} &= \frac{(\sigma_{ji}^{\parallel})^{N^{-\frac{1}{2}}} (1 - \frac{1}{2} \Delta t d_x) + c_{ijk1} D_1^{(2)} (v_k)^N}{1 + \frac{1}{2} \Delta t d_x} \\
(\sigma_{ji}^{\perp})^{N^{\frac{1}{2}}} &= (\sigma_{ji}^{\perp})^{N^{-\frac{1}{2}}} + c_{ijkl} D_l^{(2)} (v_k)^N, \quad l \neq 1 \\
(\sigma_{ij})^{N^{\frac{1}{2}}} &= (\sigma_{ij}^{\parallel})^{N^{\frac{1}{2}}} + (\sigma_{ij}^{\perp})^{N^{\frac{1}{2}}}
\end{aligned} \tag{3.21}$$

There is a summation over index  $k$  on the left-hand side of the formula for  $(\sigma_{ji}^{\parallel})^{N^{\frac{1}{2}}}$  and the summation over  $k$  and  $l$  indexes in the formula for  $(\sigma_{ji}^{\perp})^{N^{\frac{1}{2}}}$ . The staggered position of the components is not explicitly written down in 3.21, formulas work in every node of the PML layer, with the exception of the outer boundary of the PML layer, where the components can be set to zero (Dirichlet condition).

### 3.2.2 Reflection and the damping profile

The absorbing layer has a finite thickness  $\delta$ . Dirichlet boundary condition  $v_i = 0$  is set at the outer border  $x_1 = \delta$ . We will calculate the reflection coefficient for

a planar wave for the combination of both the absorbing layer and the Dirichlet boundary condition to obtain an estimate on the damping profile shape. The extensive analysis of the wave reflection in the PML layer is done in Collino and Tsogka [2001]. We will consider a simplified case in this section, with only normal incident wave.

Let the Dirichlet boundary have a reflection coefficient  $R$ , dependent on the type of incident and reflected wave and wave vector  $k_i$ . In the case of normal incident wave with  $k_2 = 0, k_3 = 0$ , the reflection coefficient is equal to 1. Phase velocity of this wave is  $v_f = \omega/k_1$ . Reflection of the whole layer is weakened by attenuation - the wave travels the distance  $\delta$  through the absorbing layer to the Dirichlet boundary and then travels back through the absorbing layer again.

The decrease in amplitude of the incident wave is given by  $\exp\left[-\frac{k_1}{\omega} \int_0^\delta d_x(s) ds\right]$ . The reflected wave propagates in the opposite direction, therefore its wave vector has opposite sign and the limits of the integration interchange, therefore the decrease in amplitude of the reflected wave is again  $\exp\left[-\frac{k_1}{\omega} \int_0^\delta d_x(s) ds\right]$ . Reflection coefficient of the whole layer is then:

$$R_{PML} = 1 \exp\left[-2\frac{k_1}{\omega} \int_0^\delta d_x(s) ds\right]. \quad (3.22)$$

Typical form of the damping profile is a power function [Komatitsch and Martin, 2007]:

$$d_x(x) = d_0 \left(\frac{x}{\delta}\right)^N, \quad (3.23)$$

where  $N > 1, d_0 > 0$  are chosen constants. Substituting (3.23) into the integral in (3.22), we get

$$R_{PML} = \exp\left[-\frac{d_0 2\delta}{v_f(N+1)}\right]. \quad (3.24)$$

We can acquire arbitrarily small reflection coefficient by increasing the value of  $d_0$ . However, this applies only for the case of continuous PDE. The discretized case (FD equations) will introduce reflections proportional to  $d_0$ , caused by the numerical numerical dispersion [Collino and Tsogka, 2001]. The concrete numerical application of PML then requires setting  $d_0$  as a compromise between both the numerical dispersion that increases the reflection, and the size of the parameters of the damping profile, that (formula 3.24) decrease it.

# Bibliography

- K. Aki and P. G. Richards. *Quantitative Seismology, 2nd Ed.* University Science Books, 2002.
- D. J. Andrews. A numerical study of tectonic stress release by underground explosions. *Bulletin of the Seismological Society of America*, 63(4), 1973.
- D. J. Andrews. Rupture velocity of plane strain shear cracks. *Journal of Geophysical Research*, 81(32), 1976. doi: 10.1029/JB081i032p05679.
- B. Barall. A grid-doubling finite-element technique for calculating dynamic three-dimensional spontaneous rupture on an earthquake fault. *Geophysical Journal International*, 178, 2009. doi: 10.1111/j.1365-246X.2009.04190.x.
- Jean-Pierre Berenger. A perfectly matched layer for the absorption of electromagnetic waves. *Journal of Computational Physics*, 114(2), 1994. doi: 10.1006/jcph.1994.1159.
- A. Bizzarri, H. S. Bhat, L. Dalguer, G. Festa, and A. Zollo. *The Mechanics of Faulting: From Laboratory to Real Earthquakes*. Research Signpost, 2012. ISBN 978-81-308-0502-3.
- R. Clayton and B. Engquist. Absorbing boundary conditions for acoustic and elastic wave equations. *Bulletin of the Seismological Society of America*, 67, 1977.
- Francis Collino and Chrysoula Tsogka. Application of the perfectly matched absorbing layer model to the linear elastodynamic problem in anisotropic heterogeneous media. *GEOPHYSICS*, 66, 2001. doi: 10.1190/1.1444908.
- V. M. Cruz-Atienza, J. Virieux, and H. Aochi. 3d finite-difference dynamic-rupture modeling along nonplanar faults. *GEOPHYSICS*, 72(5), 2007. doi: 10.1190/1.2766756.
- L. A. Dalguer and S. M. Day. Comparison of fault representation methods in finite difference simulations of dynamic rupture. *Bulletin of the Seismological Society of America*, 2006. doi: 10.1785/0120060024.
- Luis A. Dalguer and Steven M. Day. Staggered-grid split-node method for spontaneous rupture simulation. *Journal of Geophysical Research: Solid Earth*, 112 (B2), 2007.
- S. M. Day. *Finite element analysis of seismic scattering problems*. PhD thesis, California Univ., San Diego, 1977.
- S. M. Day, L. A. Dalguer, N. Lapusta, and Y. Liu. Comparison of finite difference and boundary integral solutions to three-dimensional spontaneous rupture. *Journal of Geophysical Research: Solid Earth*, 110, 2005. doi: 10.1029/2005JB003813.



- G. Di Toro, D. L. Goldsby, and T. E. Tullis. Friction falls towards zero in quartz rock as slip velocity approaches seismic rates. *Nature*, 2004. doi: 10.1038/nature02249.
- J. H. Dieterich. A model for the nucleation of earthquake slip. *Washington DC American Geophysical Union Geophysical Monograph Series*, 37, 1986. doi: 10.1029/GM037p0037.
- James H. Dieterich. Modeling of rock friction: 1. experimental results and constitutive equations. *Journal of Geophysical Research: Solid Earth*, 1979. doi: 10.1029/JB084iB05p02161.
- E. M. Dunham, D. Belanger, L. Cong, and J. E. Kozdon. Earthquake ruptures with strongly rate-weakening friction and off-fault plasticity, part 1: Planar faults. *Bulletin of the Seismological Society of America*, 101, 2011. doi: 10.1785/0120100075.
- Kenneth Duru and Eric M. Dunham. Dynamic earthquake rupture simulations on nonplanar faults embedded in 3d geometrically complex, heterogeneous elastic solids. *Journal of Computational Physics*, 305:185 – 207, 2016. doi: 10.1016/j.jcp.2015.10.021.
- A.-A. Gabriel, J.-P. Ampuero, L. A. Dalguer, and P. M. Mai. The transition of dynamic rupture styles in elastic media under velocity-weakening friction. *J. Geophys. Res.*, 117, 2012. doi: 10.1029/2012JB009468.
- M. Galis, P. M. Mai, C. Pelties, J. Kristek, P. Moczo, and J.-P. Ampuero. On the initiation of sustained slip-weakening ruptures by localized stresses. *Geophysical Journal International*, 200(2), 2014. doi: 10.1093/gji/ggu436.
- F. Gallovic, L. Valentova, J.-P. Ampuero, and A.-A. Gabriel. Bayesian dynamic finite-fault inversion: 1. method and synthetic test. *EarthArXiv*, 2019. doi: <https://doi.org/10.31223/osf.io/tmjv4>.
- D. L. Goldsby and T. E. Tullis. Flash heating leads to low frictional strength of crustal rocks at earthquake slip rates. *Science*, 334(6053), 2011. doi: 10.1126/science.1207902.
- Ellen Gottschämmer and K. B. Olsen. Accuracy of the explicit planar freesurface boundary condition implemented in a fourth-order staggered-grid velocity-stress finite-difference scheme. *Bulletin of The Seismological Society of America - BULL SEISMOL SOC AMER*, 91:617–623, 2001. doi: 10.1785/0120000244.
- R. W. Graves. Simulating seismic wave propagation in 3d elastic media using staggered-grid finite differences. *Bulletin of the Seismological Society of America*, 86:1091–1106, 08 1996.
- A. R. Harris, K. Bai, and J. P. Ampuero. A suite of exercises for verifying dynamic earthquake rupture codes. *Bulletin of the Seismological Society of America*, 2018.

- R. Harris, M. Barall, R. Archuleta, E. Dunham, B. T. Aagaard, Jean Paul Ampuero, H. Bhat, V. Cruz-Atienza, L. Dalguer, P. Dawson, S. Day, Duan , G. Ely, Y. Kaneko, Y. Kase, N. Lapusta, Y. Liu, S. Ma, D. Oglesby, and E. Templeton. The scec/usgs dynamic earthquake rupture code verification exercise. *Seismological Research Letters*, 80, 2009. doi: 10.1785/gssrl.80.1.119.
- C. Herrera, S. Ruiz, R. Madariaga, and P. Poli. Dynamic inversion of the 2015 jujuy earthquake and similarity with other intraslab events. *Geophysical Journal International*, 02 2017. doi: 10.1093/gji/ggx056.
- R. L. Higdon. Absorbing boundary conditions for elastic waves. *GEOPHYSICS*, 56(2), 1991. doi: 10.1190/1.1443035.
- Yoshiaki Ida. Stress concentration and unsteady propagation of longitudinal shear cracks. *Journal of Geophysical Research*, 1973. doi: 10.1029/JB078i017p03418.
- Y. Kaneko, N. Lapusta, and J.-P. Ampuero. Spectral element modeling of spontaneous earthquake rupture on rate and state faults: Effect of velocity-strengthening friction at shallow depths. *Journal of Geophysical Research: Solid Earth*, 113(B9), 2008. doi: 10.1029/2007JB005553.
- Dimitri Komatitsch and Roland Martin. An unsplit convolutional perfectly matched layer improved at grazing incidence for the seismic wave equation. *GEOPHYSICS*, 72, 2007. doi: 10.1190/1.2757586.
- Jozef Kristek, Peter Moczo, and Ralph J. Archuleta. Efficient methods to simulate planar free surface in the 3d 4th-order staggered-grid finite-difference schemes. *Studia Geophysica et Geodaetica*, 46(2), 2002. doi: 10.1023/A:1019866422821.
- Jozef Kristek, Peter Moczo, and Martin Galis. A brief summary of some pml formulations and discretizations for the velocity-stress equation of seismic motion. *Studia Geophysica et Geodaetica*, 53(4), 2009. doi: 10.1007/s11200-009-0034-6.
- Alan R. Levander. Fourth-order finite-difference p-sv seismograms. *GEOPHYSICS*, 53(11), 1988. doi: 10.1190/1.1442422.
- R. Madariaga. Dynamics of an expanding circular fault. *Bulletin of the Seismological Society of America*, 66(3), 1976. ISSN 0037-1106.
- R. Madariaga, K B. Olsen, and R. Archuleta. Modeling dynamic rupture in a 3d earthquake fault model. *Bulletin of the Seismological Society of America*, 88, 10 1998.
- A. Mirwald, V. M. Cruz-Atienza, J. Díaz-Mojica, A. Iglesias, S.K. Singh, C. Villafuerte, and J. Tago. The 19 september 2017 (mw7.1) intermediate-depth mexican earthquake: A slow and energetically inefficient deadly shock. *Geophysical Research Letters*, 46(4), 2019. doi: 10.1029/2018GL080904.
- P. Moczo, J. Kristek, and L. Halada. 3d fourth-order staggered-grid finite-difference schemes: Stability and grid dispersion. *Bulletin of the Seismological Society of America*, 90(3), 2000. doi: 10.1785/0119990119.

- P. Moczo, J. Robertsson, and L. Eisner. The finite-difference time-domain method for modeling of seismic wave propagation. *Advances in Geophysics*, 48, 2007. doi: 10.1016/S0065-2687(06)48008-0.
- Ch. Pelties, Y. Huang, and J.-P. Ampuero. Pulse-like rupture induced by three-dimensional fault zone flower structures. *Pure and Applied Geophysics*, 172(5), 2015. doi: 10.1007/s00024-014-0881-0.
- Z. Reches and D. A. Lockner. Fault weakening and earthquake instability by powder lubrication. *Nature*, 2010. doi: 10.1038/nature09348.
- J. R. Rice. Heating and weakening of faults during earthquake slip. *Journal of Geophysical Research: Solid Earth*, 111, 2006. doi: 10.1029/2005JB004006.
- O. Rojas, E. M. Dunham, S. M. Day, L. A. Dalguer, and J. E. Castillo. Finite difference modelling of rupture propagation with strong velocity-weakening friction. *Geophysical Journal International*, 179(3), 2009. doi: 10.1111/j.1365-246X.2009.04387.x.
- A. Ruina. Slip instability and state variable friction laws. *Journal of Geophysical Research*, 881, 1983. doi: 10.1029/JB088iB12p10359.
- T. Ulrich, A.-A. Gabriel, J.-P. Ampuero, and W. Xu. Dynamic viability of the 2016 mw 7.8 kaikōura earthquake cascade on weak crustal faults. *Nature Communications*, 10, 2019. doi: 10.1038/s41467-019-09125-w.
- J. Virieux. P-sv wave propagation in heterogeneous media: Velocity-stress finite-difference method. *GEOPHYSICS*, 51, 1986. doi: 10.1190/1.1442147.
- S. Wollherr, A.-A. Gabriel, and C. Uphoff. Off-fault plasticity in three-dimensional dynamic rupture simulations using a modal Discontinuous Galerkin method on unstructured meshes: implementation, verification and application. *Geophysical Journal International*, 214, 2018. doi: 10.1093/gji/ggy213.